J. Fluid Mech. (2022), *vol.* 940, A3, doi:10.1017/jfm.2022.191

Theoretical and numerical study of the binary scaling law for electron distribution in thermochemical non-equilibrium flows under extremely high Mach number

You Wu[1], **Xu Xu**[1,†], **Bing Chen**[1] **and Qingchun Yang**[1]

[1]School of Astronautics, Beihang University, Beijing 102206, PR China

(Received 9 June 2021; revised 14 December 2021; accepted 28 February 2022)

The binary scaling law is a classical similarity law used in analysing hypersonic flow fields. The objective of this study is to investigate the applicability of the binary scaling law in thermochemical non-equilibrium airflow. Dimensional analysis of vibrational and electron–electronic energy conservation equations was employed to explore the theoretical reasons for the failure of the binary scaling law. Numerical simulation based on a multi-temperature model (translational–rotational temperature T, electron–electronic excitation temperature T_e and the vibrational temperatures of O_2 and N_2, $T_{\upsilon_{O_2}}$ and $T_{\upsilon_{N_2}}$) with two chemical models (the Gupta model and the Park model) was adopted to study the accuracy of the binary scaling law for electron distribution at high altitude with extremely high Mach number. The results of theoretical analysis indicate that the three-body collision reactions and the translation–electron energy exchange from collisions between electrons and ions, Q_{t-e_ions}, can cause the failure of the binary scaling law. The results of numerical simulation show that the electron-impact ionization reactions are the main reasons for the invalidation of the binary scaling law for electron distribution at high altitude with high Mach number. With an increase of free-stream Mach number, the negative effect on the binary scaling law caused by Q_{t-e_ions} cannot be ignored.

Key words: hypersonic flow, laminar reacting flows

1. Introduction

Small-scale models are usually used in hypersonic testing because the complete replication of real flight conditions is not always possible. However, scale effect exists in hypersonic non-equilibrium flow and brings difficulty to experimental simulation. Similarity law plays an essential role in scaled model tests, which can ensure that the experimental results

---

† Email address for correspondence: xuxu_1521@126.com

are similar to the data in actual hypersonic flight. The binary scaling law is a classical similarity law for hypersonic and non-equilibrium flow. The binary scaling law states (Birkhoff 1960; Birkhoff & Eckerman 1963; Shen 2005) that under the same inflow static temperature T_∞ and Mach number Ma_∞, the flow fields around two scaled models are similar if the product of the incoming flow density and the characteristic size of the object $\rho_\infty L$ is equal. The binary scaling law provides enormous flexibility for high-altitude flight simulation. For instance, nozzle expansion used in creating hypersonic incoming flow in some wind tunnels can result in pressure lower than that in real flight. In order to ameliorate this problem, binary scaling can be employed to compensate for lack of pressure by using a model size larger than full scale (Hall, Eschenroeder & Marrone 1962). In addition, a reduced-scale model is usually used in order to reduce costs and pressure higher than that in flight can be employed to compensate for reduction in size according to the binary scaling law.

The binary scaling law was first proposed by Birkhoff (1960) and was called the binary collision modelling law. Two-body binary collision processes such as dissociation are characterized by $\rho_\infty L$ scaling, so the $\rho_\infty L$ scaling is termed binary scaling (Birkhoff 1960; Hornung 1972; Candler 2019). Three-body processes are characterized by $\rho_\infty^2 L$ scaling, so the fundamental reason for the failure of the binary scaling law is that three-body processes cannot be ignored (Hall *et al.* 1962; Gibson & Marrone 1964). Hall *et al.* (1962) demonstrated the practicality of the binary scaling law for a range of altitude and showed its application in hypersonic blunt-nose flows. Chemical kinetics are dominated by two-body dissociation reactions in some regimes while three-body collision processes are relatively unimportant (Hall *et al.* 1962; Hornung 1988), which is the reason why the binary scaling law is well suited for high-altitude airflow with coupled chemical non-equilibrium. Ellington (1967) examined the limitations of binary scaling for hypersonic flight and suggested that there exists a class of low-density hypersonic flows for which the binary scaling law is still applicable. Lee & Baker (1969) identified the controlling parameter for non-equilibrium air dissociation and ionization using a simplified set of boundary-layer equations and demonstrated binary scaling by comparing with axisymmetric solutions. To determine the peak electron density in the boundary layer, they provided a simple engineering means by which air ionization solutions for the axisymmetric case can be scaled to that for the angle-of-attack case. The validity of the binary scaling law was also demonstrated through analysis of a cone with constant free-stream velocity at three different altitudes (Thoenes 1969). Zhang (1990) derived the law of similarity for high-temperature real air through the analysis of the Navier–Stokes equations and explored the scaling parameters for frozen, equilibrium and non-equilibrium flows. Zeng *et al.* (2009) considered that the characteristic time of a dissociation reaction (two-body collision) is inversely proportional to free-stream density ($\tau_D \propto 1/\rho_\infty$) and the characteristic time of a recombination reaction (three-body collision) is inversely proportional to the square of free-stream density ($\tau_R \propto 1/\rho_\infty^2$). When the incoming flow density ρ_∞ decreases to a certain degree, τ_R is far greater than τ_D. If the characteristic time of flow τ_F reaches the same order of magnitude as τ_D, the three-body recombination reaction is frozen relative to the flow. Zeng (2007) also proved that scale effect does not exist in inviscid frozen airflow. Therefore, the similarity condition in this circumstance is the similarity condition for a dissociation reaction, $\rho_\infty L$. Candler (2019) reviewed the non-dimensionalization and scaling used in hypersonic flow and compared the scaling of gas–surface and gas-phase reactions.

Accurate prediction of peak heat flux is crucial to the development of hypersonic vehicles (Sivolella 2014; Zhu *et al.* 2018). The applicability of the binary scaling law in predicting heat flux was verified by wind tunnel test data of the ELECTRE vehicle under $Ma_\infty \approx 13$ (Muylaert *et al.* 1992). Camm *et al.* (1961) discussed the scaling of non-equilibrium radiation and suggested that correct scaling of radiative heat transfer requires electronic non-equilibrium to be governed by two-body collision processes. Teare, Georgiev & Allen (1962) also used binary scaling to correlate the non-equilibrium radiation from a normal shock and pointed out that radiation loss can invalidate the binary scaling concept.

The distribution and number density of electrons around hypersonic vehicles are closely related to the 'blackout' phenomenon and extra attention is paid to these conditions in entry and re-entry missions (Farbar, Boyd & Martin 2013; Ramjatan *et al.* 2020). Gibson & Marrone (1964) investigated the scaling of electron and nitric oxide concentrations using Newtonian theory and the problem of binary scaling for bluff-body flows was reduced to the simpler one of binary scaling of normal shocks. They also gave a summary of key points concerned with the range of validity of binary scaling for blunt-body flows. The prediction of peak electron number density and distribution using the binary scaling law was proved to be feasible for the ELECTRE vehicle and its scaled model under a free-stream velocity of 5530 m s^{-1} (Zeng *et al.* 2009). Zeng *et al.* 2009 proposed that the binary scaling law can be applied to all flow parameters if the incoming flow speed is in the range of 7000–11 000 m s^{-1} and $\rho_\infty L$ is less than 3×10^{-5} kg m^{-2}.

Although many scholars have undertaken research on the binary scaling law through theoretical analysis and numerical and experimental simulation, there are still some deficiencies in these works. Firstly, most theoretical analyses of the binary scaling law are limited to either kinetic theory of gases with only binary collisions considered or the mass, momentum and total energy conservation equations of the Navier–Stokes equations (Birkhoff 1960; Zhang 1990; Zeng 2007). Most previous studies did not consider thermal non-equilibrium with vibrational energy conservation equations and electron–electronic energy conservation equations. For example, translational, rotational, vibrational and electronic degrees of freedom were assumed to be fully equilibrated in the analysis of Gibson & Marrone (1964). This means that only the effects of chemical reactions (chemical non-equilibrium) on the binary scaling law were taken into account and the effects of complex energy exchange and relaxation between different energy modes (thermal non-equilibrium) were ignored. However, the effects of thermal non-equilibrium play a crucial role in hypersonic flow at high altitude. Therefore, it calls into question if there exist any other factors besides chemical three-body collisions, perhaps from energy exchange, that could theoretically cause binary scaling to fail. If such factors do exist, the extent of their contribution to the failure of the similarity law in practice must also be questioned. Secondly, although Houwing *et al.* (2000) explored the effect of vibrational non-equilibrium and modified the theoretical analysis predicting shock standoff distance, chemical dissociation and ionization effects were negligible in that study. Spacecraft enter the atmosphere at extremely high Mach number ($Ma = 30$–40) and ionization reactions are violent at extraordinarily high gas temperatures. This begs the question as to whether the binary scaling law is applicable to electron distribution under such conditions. Of all the elementary reactions in air chemistry, those which cause the binary scaling law to fail for electron distribution have yet to be identified. All of these issues mentioned above are discussed in this article.

This paper is organized as follows. Section 2 describes the physical models used in this work. Section 3 is devoted to the theoretical analysis of the binary scaling law in thermochemical non-equilibrium flows. Numerical analysis including numerical method and detailed results is presented in § 4. Conclusions are given in § 5.

2. Physical models

2.1. *Fluid governing equations*

Multi-species hypersonic reacting flows are governed by the Navier–Stokes equations with thermochemical non-equilibrium processes described by a multi-temperature model.

The continuity equation consists of a total mass equation and $(ns-1)$ species equations:

$$\frac{\partial \rho}{\partial t}+\nabla\cdot(\rho \boldsymbol{V})=0, \tag{2.1}$$

$$\frac{\partial \rho y_s}{\partial t}+\nabla\cdot(\rho y_s \boldsymbol{V})=\nabla\cdot(\rho D_s\nabla y_s)+\omega_s,\quad s=1,2,\ldots,ns-1, \tag{2.2}$$

where the index ns represents the total number of species, t is the time, ρ is the mixture density and y_s is the mass fraction of species s. Parameter $\boldsymbol{V}$ denotes the velocity and ω_s represents the source term of production of species s. Coefficient D_s is the effective diffusion coefficient of species s.

The momentum conservation equation is

$$\frac{\partial \rho \boldsymbol{V}}{\partial t}+\nabla\cdot(\rho \boldsymbol{V}\boldsymbol{V})+\nabla p=\nabla\cdot\bar{\boldsymbol{\tau}}, \tag{2.3}$$

where p is the pressure of the mixture and $\bar{\boldsymbol{\tau}}$ denotes the viscous stress tensor (Garicano-Mena, Lani & Degrez 2018).

The total energy conservation equation is

$$\frac{\partial \rho E}{\partial t}+\nabla\cdot(\boldsymbol{V}\rho H)=\nabla\cdot\left(k_{tr}\nabla T+\sum_{m=1}^{nmol}k_{v_m}\nabla T_{v_m}+k_e\nabla T_e+\bar{\boldsymbol{\tau}}\cdot\boldsymbol{V}+\sum_{s=1}^{ns}H_s\rho D_s\nabla y_s\right), \tag{2.4}$$

where E and H represent the total energy and total enthalpy per unit mass of mixture, respectively, and H_s is enthalpy per unit mass of species s. Index $nmol$ denotes the total number of molecular species. Parameters k_{tr}, k_{v_m} and k_e represent translational–rotational thermal conductivity of mixture, vibrational thermal conductivity of molecular species m and electron–electronic thermal conductivity of mixture, respectively. It is assumed that the translational temperature is equal to the rotational temperature and T denotes translational–rotational temperature. Here T_{v_m} is vibrational temperature of molecular species m. In this study, the vibrational temperature of O_2, $T_{v_{O_2}}$, and the vibrational temperature of N_2, $T_{v_{N_2}}$, are considered. The electronic–free electron modes are described by electron–electronic excitation temperature T_e.

The vibrational energy conservation equation for a non-equilibrium molecule of species m is

$$\frac{\partial \rho y_m E_{v_m}}{\partial t}+\nabla\cdot(\boldsymbol{V}\rho y_m E_{v_m})=\nabla\cdot(k_{v_m}\nabla T_{v_m}+E_{v_m}\rho D_m\nabla y_m)+\omega_{v_m}, \tag{2.5}$$

where E_{v_m} is vibrational energy per unit mass of molecular species m and ω_{v_m} represents the source term of vibrational energy of species m.

The electron–electronic energy conservation equation is

$$\frac{\partial \rho E_e}{\partial t} + \nabla \cdot (V \rho E_e) = \nabla \cdot \left(k_e \nabla T_e + \sum_{s=1}^{ns} H_{e_s} \rho D_s \nabla y_s \right) + \omega_e, \tag{2.6}$$

where E_e and H_{e_s} denote electron–electronic energy per unit mass of mixture and electron–electronic enthalpy per unit mass of species s, respectively, and ω_e represents the source term of electron–electronic energy of mixture.

2.2. *Thermodynamic relations*

The pressure of mixture is the sum of the partial pressures of each species:

$$p = \sum_{s=1}^{ns} p_s = \sum_{s \neq \mathrm{e}^-} \frac{\rho_s R_u T}{M_s} + \frac{\rho_e R_u T_e}{M_e}, \tag{2.7}$$

where p_s and M_s are the partial pressure and molecular weight of species s, respectively, M_e is the electron molecular weight and R_u is the universal gas constant.

The internal energy per unit mass of species s, i.e.

$$E_s = E_{tr_s} + E_{rot_s} + E_{v_s} + E_{e_s} + \Delta h_s, \tag{2.8}$$

is split between the translational, rotational, vibrational and electron–electronic contributions and the latent chemical energy of species s.

The translational energy and rotational energy per unit mass of species s are given by

$$E_{tr_s} = \begin{cases} \dfrac{3R_u T}{2M_s} & s \neq \mathrm{e}^- \\ 0 & s = \mathrm{e}^- \end{cases} \quad \text{and} \quad E_{rot_s} = \begin{cases} \dfrac{R_u T}{M_s} & s = dia \\ 0 & s \neq dia, \end{cases} \tag{2.9a,b}$$

where index *dia* represents diatomic molecule.

The vibrational energy and electron–electronic energy per unit mass of species s are

$$E_{v_s} = \begin{cases} \dfrac{R_u \theta_{v_s}/M_s}{\mathrm{e}^{\theta_{v_s}/T_{v_s}} - 1} & s = dia \\ 0 & s \neq dia \end{cases} \quad \text{and} \quad E_{e_s} = \begin{cases} \dfrac{\left(\dfrac{g_{1_s}}{g_{0_s}}\right) \mathrm{e}^{-\theta_{e_s}/T_e}}{1 + \left(\dfrac{g_{1_s}}{g_{0_s}}\right) \mathrm{e}^{-\theta_{e_s}/T_e}} \dfrac{R_u \theta_{e_s}}{M_s} & s \neq \mathrm{e}^- \\ \dfrac{3R_u T_e}{2M_e} & s = \mathrm{e}^-, \end{cases} \tag{2.10a,b}$$

where θ_{v_s} and θ_{e_s} denote the characteristic vibrational temperature and the characteristic electronic temperature of species s, respectively, and g_{0_s} and g_{1_s} are the degeneracy of the ground and the first electronic level of species s, respectively.

2.3. *Chemistry model*

This study selects the Gupta chemical reaction model (Gupta *et al.* 1990) and the Park model (Park 1993) which are applied to 11 air species (O_2, N_2, N, O, NO, N^+, O^+,

N_2^+, O_2^+, NO^+, e^-). The mass production rate ω_s is calculated by

$$\omega_s = M_s \sum_{z=1}^{nr} (\nu_{z,s}^b - \nu_{z,s}^f) R_z^{fb} = M_s \sum_{z=1}^{nr} (\nu_{z,s}^b - \nu_{z,s}^f)(R_z^f - R_z^b), \tag{2.11}$$

where $\nu_{z,s}^f$ and $\nu_{z,s}^b$ are the stoichiometric coefficients of species s for the reactants and products in reaction z, respectively, and R_z^{fb} denotes the total reaction rate of reaction z. The forward and backward reaction rates can be written as

$$R_z^f = \Gamma_z k_z^f \prod_{l=1}^{ns} \left(\frac{\rho_l}{M_l}\right)^{\nu_{z,l}^f}, \quad R_z^b = \Gamma_z k_z^b \prod_{l=1}^{ns} \left(\frac{\rho_l}{M_l}\right)^{\nu_{z,l}^b}, \tag{2.12a,b}$$

where Γ_z is given as follows:

$$\Gamma_z = \left[\sum_{l=1}^{ns} \alpha_{z,l} \left(\frac{\rho_l}{M_l}\right)\right]^{L_z}, \tag{2.13}$$

where $\alpha_{z,l}$ denotes the third-body efficiency for species l in reaction z. Here L_z equals 1 when a third body M is needed in reaction z. Otherwise, L_z equals 0.

When the Gupta model is employed, the forward and backward reaction rate coefficients, k_z^f and k_z^b, are expressed in modified Arrhenius form as

$$k_z^f = A_{f,z} T_f^{B_{f,z}} \mathrm{e}^{-C_{f,z}/T_f}, \quad k_z^b = A_{b,z} T_b^{B_{b,z}} \mathrm{e}^{-C_{b,z}/T_b}, \tag{2.14a,b}$$

where T_f and T_b represent the controlling temperature of the forward and backward reactions, respectively. When the Park model is applied, k_z^f is still calculated by (2.14*a*,*b*) and k_z^b is obtained by the equilibrium constant (Park 1985):

$$k_z^b = \frac{k_z^f(T_b)}{K_{eq,z}(T_b)}, \tag{2.15}$$

where the equilibrium constant $K_{eq,z}$ is given as the following curve-fitting expression (Park 1990):

$$K_{eq,z}(T_b) = exp\left(\frac{A_1^z}{S} + A_2^z + A_3^z \ln S + A_4^z S + A_5^z S^2\right), \tag{2.16}$$

where $S = 10\,000/T_b$ and the constants $A_1^z, A_2^z, A_3^z, A_4^z, A_5^z$ are given by Park (1990). Those five constants for $N_2 + N^+ \rightleftharpoons N + N_2^+$ are not included in Park (1990), so the equilibrium constant $K_{eq,z}$ for $N_2 + N^+ \rightleftharpoons N + N_2^+$ is calculated using the similar method proposed by Park (1985) and Ghezali, Haoui & Chpoun (2019). Radiative recombination reactions in the Park model are not considered, because radiation is ignored in this paper.

2.4. *Energy exchange model*

The vibrational energy source term of molecular species m can be decomposed as

$$\omega_{v_m} = Q_{t-v_m} + Q_{v-v_m} + Q_{e-v_m} + Q_{r-v_m}, \tag{2.17}$$

where Q_{t-v_m} denotes the energy exchange between translation and vibration energies. Energy exchange Q_{t-v_m} is evaluated using Landau–Teller theory (Landau & Teller 1936) as

$$Q_{t-v_m} = \rho y_m \frac{E_{v_m}(T) - E_{v_m}(T_{v_m})}{\tau_{vt,m}}, \tag{2.18}$$

and the relaxation time of vibration–translation exchanges $\tau_{vt,m}$ modelled by the Millikan–White empirical formula (Millikan & White 1963; Miller *et al.* 1995) is expressed as

$$\tau_{vt,m}^{MW} = \sum_{s \neq \mathrm{e}^-} X_s \Big/ \sum_{s \neq \mathrm{e}^-} \frac{X_s}{\tau_{vt,m,s}}, \tag{2.19}$$

$$\tau_{vt,m,s} = \frac{101\ 325}{p} exp[a_{m,s}(T^{-1/3} - b_{m,s}) - 18.42], \tag{2.20}$$

where X_s is the mole fraction of heavy particle s. Here $a_{m,s}$ and $b_{m,s}$ are given by

$$a_{m,s} = 0.00116\mu_{m,s}^{1/2}\theta_{v_m}^{4/3}, \tag{2.21}$$

$$b_{m,s} = 0.015\mu_{m,s}^{1/4}, \tag{2.22}$$

where the reduced mass $\mu_{m,s}$ is defined as

$$\mu_{m,s} = \frac{1000 M_m M_s}{M_m + M_s}. \tag{2.23}$$

When the temperature is higher than 8000 K, Park (1990) suggests that the correction term should be added on the basis of $\tau_{vt,m}^{MW}$ and the total relaxation time $\tau_{vt,m}$ can be expressed as

$$\tau_{vt,m} = \tau_{vt,m}^{MW} + (\sigma_m \bar{C}_m n_m)^{-1}, \tag{2.24}$$

where the average molecular velocity $\bar{C}_m$, the effective cross-section σ_m and number density n_m of species m are given by

$$\bar{C}_m = \left(\frac{8R_u T}{\pi M_m}\right)^{1/2}, \tag{2.25}$$

$$\sigma_m = 10^{-21}\left(\frac{50\ 000}{T}\right)^2, \tag{2.26}$$

$$n_m = \frac{\rho y_m N_0}{M_m}, \tag{2.27}$$

where N_0 is Avogadro's constant. Time $\tau_{vt,m}$ can be expressed as

$$\tau_{vt,m} = f_{\tau_{vt,m}}(\rho, T, y_1, \ldots, y_{ns}) = \frac{1}{\rho} f'_{\tau_{vt,m}}(T, T_e, y_1, \ldots, y_{ns}), \tag{2.28}$$

where $f_{\tau_{vt,m}}$ stand for the functions by which $\tau_{vt,m}$ can be calculated. The term $f'_{\tau_{vt,m}}$ does not involve the density ρ. Thus, the term Q_{t-v_m} can be written as

$$Q_{t-v_m} = \rho^2 f'_{Q_{t-v_m}}(T, T_{v_m}, T_e, y_1, \ldots, y_{ns}), \tag{2.29}$$

where $f'_{Q_{t-v_m}}$ is independent of ρ.

The vibrational energy exchange between the different molecules Q_{v-v_m} is described according to Roberts (1994):

$$Q_{v-v_m} = \frac{\rho y_m}{M_m} \sum_{s=1, s \neq m}^{mol} \left\{ \frac{X_s}{\tau_{vv,m,s}} \left[\frac{1 - exp\left(-\frac{\theta_{vm}}{T}\right)}{1 - exp\left(-\frac{\theta_{vs}}{T}\right)} \right] \frac{e_{v_s}(T_{v_s})}{e_{v_s}(T)} [e_{v_m}(T) - e_{v_m}(T_{v_m})] \right.$$
$$\left. - \frac{X_s}{\tau_{vv,m,s}} \frac{e_{v_m}(T_{v_m})}{e_{v_s}(T)} [e_{v_s}(T) - e_{v_s}(T_{v_s})] \right\}, \tag{2.30}$$

where e_{v_m} denotes the vibrational energy per mole of species m. Note that species m can only be N_2 in (2.30). For other species, the transfer of vibrational energy can be obtained according to the assumption of conservation of vibrational energy (Miller *et al.* 1995). The relaxation time of vibration–vibration exchanges $\tau_{vv,m,s}$ can be written as

$$\tau_{vv,m,s} = \frac{1}{P_{m,s}(8\pi KTN_0/\mu_{m,s})^{1/2}\sigma_{m,s}^2 n_s}, \tag{2.31}$$

where K and $\sigma_{m,s}$ represent Boltzmann's constant and the collision cross-sections (Miller *et al.* 1995), respectively. The probability of energy transfer during each collision $P_{m,s}$ is provided by Park (1993) as

$$P_{\mathrm{N_2,NO}} = 5.5 \times 10^{-5} \left(\frac{T}{1000}\right)^{2.32}, \tag{2.32}$$

$$P_{\mathrm{N_2,O_2}} = 3.0 \times 10^{-6} \left(\frac{T}{1000}\right)^{2.87}. \tag{2.33}$$

In this paper, only collision between N_2 and O_2 is taken into consideration. Like Q_{t-v_m}, the term Q_{v-v_m} can be expressed as

$$Q_{v-v_m} = \rho^2 f'_{Q_{v-vm}}(T, T_{v_m}, y_m, y_{s1}, \ldots, y_{smol}), \tag{2.34}$$

where $y_{s1}, \ldots, y_{smol}$ represent the molecular species except species m.

The energy exchange between vibrational and electronic modes Q_{e-v_m} is modelled as (Candler & Maccormack 1991)

$$Q_{e-v_m} = \rho y_m \frac{E_{v_m}(T_e) - E_{v_m}(T_{v_m})}{\tau_{e,m}}, \tag{2.35}$$

where $\tau_{e,m}$ denotes the relaxation time of electronic–vibrational exchanges for species m. Parameter $\tau_{e,\mathrm{N_2}}$ is given based on research of Lee (1993) and Candler (1988) by

$$\log_{10}\left(\frac{p_e \tau_{e,\mathrm{N_2}}}{101\ 325}\right) = 3.91 \log_{10}^2(T_e) - 30.36\log_{10}(T_e) + 48.90, \quad 1000\ \mathrm{K} \leq T_e \leq 7000\ \mathrm{K}, \tag{2.36}$$

$$\log_{10}\left(\frac{p_e \tau_{e,\mathrm{N_2}}}{101\ 325}\right) = 1.30 \log_{10}^2(T_e) - 9.09\log_{10}(T_e) + 5.58, \quad 7000 < T_e \leq 50\ 000\ \mathrm{K}, \tag{2.37}$$

where p_e is the electron partial pressure.

Parameter τ_{e,O_2} is obtained from the formula of Park & Lee (1995) based on τ_{e,N_2}:

$$\tau_{e,\mathrm{O}_2} = 300 \times \tau_{e,\mathrm{N}_2}(1.492T_e). \tag{2.38}$$

The term Q_{e-v_m} can also be written as

$$Q_{e-v_m} = \rho^2 f'_{Q_{e-v_m}}(T, T_e, y_m, y_{\mathrm{e}^-}), \tag{2.39}$$

where $f'_{Q_{e-v_m}}$ does not depend on ρ.

The change in vibrational energy due to chemical reactions Q_{r-v_m} can be expressed as (Miller *et al.* 1995)

$$Q_{r-v_m} = \omega_m E_{v_m}. \tag{2.40}$$

The electron–electronic energy source term can be decomposed as

$$\omega_e = Q_{t-e} - \sum_{m=mol} Q_{e-v_m} + Q_{r-e} + Q_{i-e} - p_e \nabla \cdot \boldsymbol{V}. \tag{2.41}$$

The energy exchange between translation and electron modes Q_{t-e} can be written as (Miller *et al.* 1995; Roberts 1996)

$$Q_{t-e} = 3\rho_e R_u (T - T_e) \sum_{s \neq \mathrm{e}^-} \frac{v_{e,s}}{M_s}, \tag{2.42}$$

where $v_{e,s}$ denotes the collision frequency between electrons and species s. For ions and electrons, it follows Coulomb collisions and can be expressed as (Appleton & Bray 1964)

$$v_{e,s} = \frac{8}{3}\left(\frac{\pi}{m_e}\right)^{1/2} n_s e_c^4 \frac{1}{(2KT_e)^{3/2}} \ln\left(\frac{K^3 T_e^3}{\pi n_e e_c^6}\right), \tag{2.43}$$

where m_e is the electron mass, n_e denotes number density of electrons and e_c is the magnitude of the electronic charge. For collisions between neutral species and electrons, the collision frequency can be expressed as (Appleton & Bray 1964)

$$v_{e,s} = n_s \sigma_{e,s} \left(\frac{8KT_e}{\pi m_e}\right)^{1/2}, \tag{2.44}$$

where the effective cross-section $\sigma_{e,s}$ is evaluated by curve fits (Gnoffo, Gupta & Shinn 1989) as

$$\sigma_{e,s} = a_s + b_s T_e + c_s T_e^2. \tag{2.45}$$

The collision frequency $v_{e,s}$ and the effective cross-section $\sigma_{e,s}$ can also be calculated by similar formulae obtained by Petschek & Byron (1957) or Matsuzaki (1988) and the simulation in § 4 uses Matsuzaki's model. Regardless of the model mentioned, the term Q_{t-e} can be written as

$$\begin{aligned} Q_{t-e} &= Q_{t-e\_neu} + Q_{t-e\_ions} \\ &= \rho^2 [f^{neu}_{t-e}(T, T_e, y_{\mathrm{e}^-}, y_{neu1}, \ldots, y_{neun}) + f^{ion}_{t-e}(\rho, T, T_e, y_{\mathrm{e}^-}, y_{ion1}, \ldots, y_{ionn})] , \end{aligned} \tag{2.46}$$

where Q_{t-e_neu} denotes the translation–electron energy exchange from collisions between electrons and neutral particles and Q_{t-e_ions} denotes that from collisions between electrons and ions. The term f^{neu}_{t-e} represents the contribution of the electron–neutral particle collisions and is not correlated with ρ; f_{t-e}^{ion} stands for the contribution of the electron–ion collisions and depends on ρ.

The added or removed electron energy due to chemical reactions Q_{r-e} can be specified as (Hao, Wang & Lee 2016)

$$Q_{r-e} = \sum_{s=1}^{ns} \omega_s E_{e_s}. \tag{2.47}$$

The term Q_{i-e} represents the energy loss of free electrons by the impact ionization reactions (Scalabrin 2007), which gives

$$Q_{i-e} = -\tfrac{1}{3}(I_{\mathrm{O}}\omega_{\mathrm{O}^+} + I_{\mathrm{N}}\omega_{\mathrm{N}^+}), \tag{2.48}$$

where I_{O} and I_{N} are the first energy of ionization of O and N; ω_{O^+} and ω_{N^+} are the formation rate of O^+ and N^+ in the electron-impact ionization reactions.

The term $-p_e\nabla \cdot \boldsymbol{V}$ denotes the contribution of electron partial pressure in electron–electronic energy change (Gnoffo *et al.* 1989; Lee 1984).

2.5. *Transport properties*

The dynamic viscosity coefficient of each species is obtained by curve fits taken from Gupta *et al.* (1990) in the temperature range (1000–30 000 K) and Lennard-Jones potential (Anderson 2006) in the other temperature range. The translational–rotational, vibrational and electron–electronic thermal conductivities of each species are given by Eucken's relation (Anderson 2006). The dynamic viscosity μ and thermal conductivities of gas mixture are derived from Wilke's rule (Wilke 1950). So μ, k_{tr}, k_{v_m} and k_e can be expressed as

$$\mu = f_{\mu}(T, T_e, y_1, \ldots, y_{ns}), \tag{2.49}$$

$$k_{tr} = f_{k_{tr}}(T, y_1, \ldots, y_{ns}), \tag{2.50}$$

$$k_{v_m} = f_{k_{v_m}}(T, T_{v_m}, y_1, \ldots, y_{ns}), \tag{2.51}$$

$$k_e = f_{k_e}(T, T_e, y_1, \ldots, y_{ns}), \tag{2.52}$$

where f_{μ}, $f_{k_{tr}}$, $f_{k_{v_m}}$ and f_{k_e} stand for the functions by which μ, k_{tr}, k_{v_m} and k_e can be calculated, respectively. One can observe that μ, k_{tr}, k_{v_m} and k_e depend on temperatures and mass fraction of each species.

It is assumed that the binary diffusion coefficients between each pair of components D_{sj} are the same and the electric current of the flow field is zero. The multi-component diffusion coefficient of each species D_s is given as follows:

$$D_s = \begin{cases} \dfrac{(1-y_s)\mu}{\rho(1-X_s)Sc} & s \neq \mathrm{e}^-, \\[2ex] \dfrac{\sum_{s=1}^{nion} y_s D_s}{\sum_{s=1}^{nion} y_s} & s = \mathrm{e}^-, \end{cases} \tag{2.53}$$

where Sc is the Schmidt number and index *nion* denotes the total number of ion species. For neutral particles, $Sc = 0.5$. For ions, $Sc = 0.25$. In a similar way, D_s can also be expressed as

$$D_s = f_{D_s}(T, T_e, \rho, y_1, \ldots, y_{ns}) = f'_{D_s}(T, T_e, y_1, \ldots, y_{ns})/\rho, \tag{2.54}$$

where the functions f_{D_s} and f'_{D_s} show that D_s depends on density, temperature and mass fraction of each species.

3. The binary scaling law in thermochemical non-equilibrium

The binary scaling law requires the same $\rho_\infty L$, T_∞, U_∞ for two different flows and the mass fractions of free streams $y_{1,\infty}, \ldots, y_{ns,\infty}$ also need to be consistent. Flow parameters need to be transformed to the dimensionless form for similarity analysis (see Appendix A). By analysing the dimensionless continuity, momentum conservation and total energy conservation equation, the similarity law for real gas flow is given by Zhang (1990). In this paper, the similarity analysis based on the dimensionless vibrational and electron–electronic energy conservation equation is discussed in detail.

Radiation and ablation might become important at large Mach number. Teare *et al.* (1962) considered that, in a certain range of altitude and free-stream velocity, the intensity of radiation is proportional to the particle density when two-body collision processes prevail sufficiently. If the condition of the binary scaling law ($\rho_\infty R = \text{const.}$) is satisfied, the integrated radiation flux emitted from the non-equilibrium region is independent of the particle density and binary scaling is applicable to radiation (Camm *et al.* 1961; Teare *et al.* 1962). Zeng *et al.* (2009) investigated the radiation of re-entry flows at $U_\infty = 7650,\ 11\,360\ \text{m s}^{-1}$ and the results revealed that non-equilibrium radiation abides by the binary scaling law. However, the binary scaling law is invalid for analysing radiation in some extreme cases (Teare *et al.* 1962; Zeng *et al.* 2009). Ablation involves various gas–surface reactions. The scaling of the gas–surface reactions is not as clear as that of the gas-phase reactions (Candler 2019). The rates of gas–surface reactions depend on the fraction of active sites in a certain phase (Marschall & MacLean 2011). For example, the catalytic recombination of nitrogen $\text{N} + \text{N(s)} \rightleftharpoons \text{N}_2$ is one of the basic gas–surface reactions. Here, N(s) denotes a nitrogen atom that is bonded to an open surface site. The rate of this reaction depends on both the gas-phase N atom concentration and the number of N atoms bonded to the surface sites (Candler 2019). Thus, both radiation and ablation might inhibit the binary scaling. However, this article aims to investigate the effects of energy exchange and air reactions on the binary scaling law. To avoid interference, radiation and ablation are not considered in this paper. Thus, the simplest wall boundary condition, i.e. an isothermal and fully catalytic wall boundary, is employed in similarity analysis.

3.1. *Similarity analysis for continuity equation*

The analysis based on the dimensionless continuity equation (Zhang 1990) is reviewed first:

$$\frac{\partial \bar{\rho} y_s}{\partial \bar{t}} + \frac{\partial \bar{\rho} y_s \bar{u}_j}{\partial \bar{x}_j} = \frac{1}{Re_\infty} \frac{\partial \left(\frac{\bar{\rho} \bar{D}_s \partial y_s}{\partial \bar{x}_j} \right)}{\partial \bar{x}_j} + \frac{L}{\rho_\infty U_\infty} \omega_s, \tag{3.1}$$

where the overbar is used to denote non-dimensional variables. Parameter $\bar{D}_s$ can be expressed in the following form (see (2.49), (2.54) and (A4), (A5) in Appendix A):

$$\bar{D}_s = \frac{f'_{D_s}(\bar{T}T_\infty, \bar{T}_e T_\infty, y_1, \ldots, y_{ns})/\rho}{f_\mu(T_\infty, T_{e,\infty}, y_{1,\infty}, \ldots, y_{ns,\infty})/\rho_\infty} = \frac{f'_{D_s,T_\infty}(\bar{T}, \bar{T}_e, y_1, \ldots, y_{ns})}{f_{\mu,T_\infty}(1, T_{e,\infty}/T_\infty, y_{1,\infty}, \ldots, y_{ns,\infty})\bar{\rho}}, \tag{3.2}$$

where the index T_∞ represents that the functions f_{μ,T_∞} and f'_{D_s,T_∞} are relevant to the temperature of free stream T_∞. Formula (3.2) shows that $\bar{D}_s$ only depends on dimensional parameter T_∞ in addition to non-dimensional parameters.

The second item on the right-hand side of (3.1) can be written as

$$\begin{aligned} rhs_{c2} &= \frac{L}{\rho_\infty U_\infty} M_s \sum_{z=1}^{nr} (\nu^b_{z,s} - \nu^f_{z,s}) \left[\sum_{l=1}^{ns} \alpha_{z,l} \left(\frac{\rho_l}{M_l}\right)\right]^{L_z} \left[k^f_z \prod_{l=1}^{ns} \left(\frac{\rho_l}{M_l}\right)^{\nu^f_{z,l}} - k^b_z \prod_{l=1}^{ns} \left(\frac{\rho_l}{M_l}\right)^{\nu^b_{z,l}}\right] \\ &= \frac{\rho_\infty L}{U_\infty} M_s \sum_{z=1}^{nr} (\nu^b_{z,s} - \nu^f_{z,s}) \left[\sum_{l=1}^{ns} \alpha_{z,l} \left(\frac{y_l}{M_l}\right)\right]^{L_z} \left[k^f_z \bar{\rho}^{L_z + \sum_{l=1}^{ns} \nu^f_{z,l}} \rho_\infty^{L_z + \sum_{l=1}^{ns} \nu^f_{z,l} - 2} \prod_{l=1}^{ns} \left(\frac{y_l}{M_l}\right)^{\nu^f_{z,l}} \right. \\ &\quad \left. - k^b_z \bar{\rho}^{L_z + \sum_{l=1}^{ns} \nu^b_{z,l}} \rho_\infty^{L_z + \sum_{l=1}^{ns} \nu^f_{z,l} - 2} \prod_{l=1}^{ns} \left(\frac{y_l}{M_l}\right)^{\nu^b_{z,l}}\right] \\ &= \frac{\rho_\infty L}{U_\infty} M_s \sum_{z=1}^{nr} (\nu^b_{z,s} - \nu^f_{z,s}) \left[\sum_{l=1}^{ns} \alpha_{z,l} \left(\frac{y_l}{M_l}\right)\right]^{L_z} R'_z, \end{aligned} \tag{3.3}$$

where $\rho_\infty L$ and U_∞ are each required to be the same between two different flows according to the binary scaling law. Terms k^f_z and k^b_z can be expressed as a function of dimensionless parameters like $\bar{D}_s$:

$$k^{f/b}_z = f_{k^{f/b}_z}(T, T_e, T_{v_1}, \ldots, T_{v_{mol}}) = f_{k^{f/b}_z, T_\infty}(\bar{T}, \bar{T}_e, \bar{T}_{v_1}, \ldots, \bar{T}_{v_{mol}}). \tag{3.4}$$

As far as elementary reactions of high-temperature air are concerned (Gupta *et al.* 1990; Park 1993), the forward reactions can be only second-order reactions and the backward reactions can be either second-order or third-order reactions. When the reverse of reaction z is a second-order reaction, $L_z + \sum_{l=1}^{ns} \nu^f_{z,l} = 2$ and $L_z + \sum_{l=1}^{ns} \nu^b_{z,l} = 2$ in (3.3). Thus, R'_z in (3.3) can be written as (refer to (3.4))

$$\begin{aligned} R'_z &= k^f_z \bar{\rho}^2 \prod_{l=1}^{ns} \left(\frac{y_l}{M_l}\right)^{\nu^f_{z,l}} - k^b_z \bar{\rho}^2 \prod_{l=1}^{ns} \left(\frac{y_l}{M_l}\right)^{\nu^b_{z,l}} \\ &= f_{R'_z, T_\infty}(\bar{\rho}, \bar{T}, \bar{T}_e, \bar{T}_{v_1}, \ldots, \bar{T}_{v_{mol}}, y_1, \ldots, y_{ns}), \end{aligned} \tag{3.5}$$

where $f_{R'_z, T_\infty}$ only depends on the dimensional parameter T_∞ in addition to dimensionless parameters.

When the reverse of reaction z is a third-order reaction, $L_z + \sum_{l=1}^{ns} \nu^f_{z,l} = 2$ and $L_z + \sum_{l=1}^{ns} \nu^b_{z,l} = 3$. Therefore, R'_z can be expressed as

$$\begin{aligned} R'_z &= k^f_z \bar{\rho}^2 \prod_{l=1}^{ns} \left(\frac{y_l}{M_l}\right)^{\nu^f_{z,l}} - k^b_z \bar{\rho}^3 \rho_\infty \prod_{l=1}^{ns} \left(\frac{y_l}{M_l}\right)^{\nu^b_{z,l}} \\ &= f_{R'_z, T_\infty, \rho_\infty}(\bar{\rho}, \bar{T}, \bar{T}_e, \bar{T}_{v_1}, \ldots, \bar{T}_{v_{mol}}, y_1, \ldots, y_{ns}), \end{aligned} \tag{3.6}$$

where $f_{R'_z,T_\infty,\rho_\infty}$ depends on both T_∞ and ρ_∞ in addition to dimensionless parameters. In this case, the similarity between two different hypersonic airflows not only needs the same $\rho_\infty L$ but also needs the same ρ_∞. In other words, the scale of the flow field L needs to be equal everywhere and the two flows are actually the same.

Generally, the density ρ of the flow field around hypersonic vehicles is relatively low because of the low density of the free stream ρ_∞ at high altitude. In this case, the backward third-order reaction rate is far less than the forward second-order reaction rate for reaction z in most areas of the flow field. Thus, for high-altitude flow, formula (3.6) can be written as follows:

$$\begin{aligned} R'_z &= k_z^f \bar{\rho}^2 \prod_{l=1}^{ns} \left(\frac{y_l}{M_l}\right)^{\nu_{z,l}^f} - \rho \left[k_z^b \bar{\rho}^2 \prod_{l=1}^{ns} \left(\frac{y_l}{M_l}\right)^{\nu_{z,l}^b} \right] \approx k_z^f \bar{\rho}^2 \prod_{l=1}^{ns} \left(\frac{y_l}{M_l}\right)^{\nu_{z,l}^f} \\ &= f'_{R'_z,T_\infty}(\bar{\rho}, \bar{T}, \bar{T}_e, \bar{T}_{v_1}, \ldots, \bar{T}_{v_{mol}}, y_1, \ldots, y_{ns}), \end{aligned} \tag{3.7}$$

where $f'_{R'_z,T_\infty}$ is unrelated to ρ_∞. In this case, should $\rho_\infty L,\ T_\infty,\ U_\infty,\ y_{1,\infty}, \ldots, y_{ns,\infty}$ be identical, the airflows over geometrically similar objects will be similar and the binary scaling law can be applied to the continuity equation.

3.2. *Similarity analysis for vibrational energy conservation equation*

The dimensionless vibrational energy conservation equation is written as

$$\frac{\partial \bar{\rho} y_m \bar{E}_{v_m}}{\partial \bar{t}} + \frac{\partial \bar{\rho} y_m \bar{E}_{v_m} \bar{u}_j}{\partial \bar{x}_j} = \frac{1}{Re_\infty} \frac{\partial \left(\bar{k}_{v_m} \frac{\partial \bar{T}_{v_m}}{\partial \bar{x}_j} + \bar{\rho} \bar{D}_m \bar{E}_{v_m} \frac{\partial y_m}{\partial \bar{x}_j} \right)}{\partial \bar{x}_j} + \frac{L}{\rho_\infty U_\infty^3} \omega_{v_m}, \tag{3.8}$$

where $\bar{k}_{v_m}$ and $\bar{E}_{v_m}$ can be expressed as follows (see (2.49), (2.51) and (A3), (A6) in Appendix A):

$$\bar{k}_{v_m} = \frac{f_{k_{v_m}}(T, T_{v_m}, y_1, \ldots, y_{ns})}{\mu_\infty U_\infty^2 / T_\infty} = \frac{f_{k_{v_m},T_\infty}(\bar{T}, \bar{T}_{v_m}, y_1, \ldots, y_{ns})}{f_{\mu,T_\infty}(1, T_{e,\infty}/T_\infty, y_{1,\infty}, \ldots, y_{ns,\infty}) U_\infty^2 / T_\infty}, \tag{3.9}$$

$$\bar{E}_{v_m} = \frac{f_{E_{v_m},T_\infty}(\bar{T}_{v_m})}{U_\infty^2}. \tag{3.10}$$

Formulae (3.9) and (3.10) indicate that T_∞ and U_∞ are the only dimensional parameters on which $\bar{k}_{v_m}$ and $\bar{E}_{v_m}$ depend. The second item on the right-hand side of (3.8) can be written as (refer to (2.29), (2.34), (2.39) and (2.40))

$$\begin{aligned} rhs_{v2} &= \frac{\rho_\infty L}{\rho_\infty^2 U_\infty^3}(Q_{t-v_m} + Q_{v-v_m} + Q_{e-v_m} + Q_{r-v_m}) = \frac{\rho_\infty L}{U_\infty^3}(\bar{\rho}^2 f'_{Q_{t-v_m}} + \bar{\rho}^2 f'_{Q_{v-v_m}} \\ &\quad + \bar{\rho}^2 f'_{Q_{e-v_m}}) + \frac{L}{\rho_\infty U_\infty^3} \omega_m E_{v_m}, \end{aligned} \tag{3.11}$$

where $f'_{Q_{t-v_m}}$ can be written as a function of dimensionless parameters by (2.29):

$$f'_{Q_{t-v_m}} = f'_{Q_{t-v_m},T_\infty}(\bar{T}, \bar{T}_{v_m}, \bar{T}_e, y_1, \cdots, y_{ns}), \tag{3.12}$$

where $f'_{Q_{t-v_m},T_\infty}$ only depends on dimensional parameter T_∞ besides dimensionless parameters. Similarly, $f'_{Q_{v-v_m}}$ and $f'_{Q_{e-v_m}}$ can also be expressed as functions

$f'_{Q_{v-v_m,T_\infty}}(\bar{T}, \bar{T}_{v_m}, y_m, y_{s1}, \ldots, y_{smol})$ and $f'_{Q_{e-v_m,T_\infty}}(\bar{T}, \bar{T}_e, y_m, y_{\mathrm{e}^-})$, which are only related to dimensional parameter T_∞. These three terms can ensure the similarity of the vibrational energy conservation equation when the preconditions of the binary scaling law are satisfied. The term $(L/\rho_\infty U_\infty^3)\omega_m E_{v_m}$ can be analogous to the term $(L/\rho_\infty U_\infty)\omega_s$ in continuity equation (3.1) and depends on both T_∞ and ρ_∞. Thus, the term $(L/\rho_\infty U_\infty^3)\omega_m E_{v_m}$ can cause dissimilarity in two hypersonic airflows which have different scales but meet the conditions of the binary scaling law. The fundamental cause of this dissimilarity also lies in the three-body reactions of the reverse reaction. Just as in the continuity equation (3.1), the binary scaling law can be applied to the vibrational energy conservation equation as long as the incoming flow density ρ_∞ is low enough.

Thus, only Q_{r-v_m} in the vibrational energy conservation equation can theoretically result in the failure of the binary scaling law and the root cause is still three-body reactions.

3.3. *Similarity analysis for electron–electronic energy conservation equation*

The dimensionless electron–electronic energy conservation equation is written as

$$\frac{\partial \bar{\rho}\bar{E}_e}{\partial \bar{t}} + \frac{\partial \bar{\rho}\bar{E}_e \bar{u}_j}{\partial \bar{x}_j} = \frac{1}{Re_\infty}\frac{\partial\left(\bar{k}_e \frac{\partial \bar{T}_e}{\partial \bar{x}_j} + \bar{\rho}\sum_{s=1}^{ns}\bar{D}_s \bar{H}_{e_s}\frac{\partial y_s}{\partial \bar{x}_j}\right)}{\partial \bar{x}_j} + \frac{L}{\rho_\infty U_\infty^3}\omega_e, \tag{3.13}$$

where $\bar{k}_e$, $\bar{E}_e$ and $\bar{H}_{e_s}$ can be expressed as follows (see (2.49), (2.52) and (A3), (A6) in Appendix A):

$$\bar{k}_e = \frac{f_{k_e}(T, T_e, y_1, \ldots, y_{ns})}{\mu_\infty U_\infty^2/T_\infty} = \frac{f_{k_e,T_\infty}(\bar{T}, \bar{T}_e, y_1, \ldots, y_{ns})}{f_{\mu,T_\infty}(1, T_{e,\infty}/T_\infty, y_{1,\infty}, \ldots, y_{ns,\infty})U_\infty^2/T_\infty}, \tag{3.14}$$

$$\bar{E}_e = \frac{f_{E_e,T_\infty}(\bar{T}_e, y_1, \ldots, y_{ns})}{U_\infty^2}, \tag{3.15}$$

$$\bar{H}_{e_s} = \frac{f_{H_{e_s},T_\infty}(\bar{T}_e)}{U_\infty^2}. \tag{3.16}$$

Similar to $\bar{k}_{v_m}$ and $\bar{E}_{v_m}$ in § 3.2, the dimensional parameters on which $\bar{k}_e$, $\bar{E}_e$ and $\bar{H}_{e_s}$ depend are only T_∞ and U_∞. The second item on the right-hand side of (3.13) can be written as (refer to (2.39), (2.46), (2.47) and (2.48))

$$\begin{aligned} rhs_{e2} &= \frac{\rho_\infty L}{\rho_\infty^2 U_\infty^3}\left(Q_{t-e} - \sum_{m=mol} Q_{e-v_m} + Q_{r-e} + Q_{i-e} - p_e\frac{\partial u_j}{\partial x_j}\right) \\ &= \frac{\rho_\infty L}{U_\infty^3}\left(\bar{\rho}^2 f_{t-e}^{ion} + \bar{\rho}^2 f_{t-e}^{neu} - \bar{\rho}^2 \sum_{m=mol} f'_{Q_{e-v_m}}\right) \\ &\quad + \frac{L}{\rho_\infty U_\infty^3}\left(\sum_{s=1}^{ns}\omega_s E_{e_s} - \frac{1}{3}(I_{\mathrm{O}}\omega_{\mathrm{O}^+} + I_{\mathrm{N}}\omega_{\mathrm{N}^+})\right) - \frac{Lp_e}{\rho_\infty U_\infty^3}\frac{\partial u_j}{\partial x_j}, \end{aligned} \tag{3.17}$$

where f_{t-e}^{ion} and f_{t-e}^{neu} can be written as functions $f_{t-e,T_\infty,\rho_\infty}^{ion}(\bar{\rho}, \bar{T}, \bar{T}_e, y_{\mathrm{e}^-}, y_{ion1}, \ldots, y_{ionn})$ and $f_{t-e,T_\infty}^{neu}(\bar{T}, \bar{T}_e, y_{\mathrm{e}^-}, y_{neu1}, \ldots, y_{neun})$, respectively, based on (2.46), similar to $f'_{Q_{e-v_m,T_\infty}}(\bar{T}, \bar{T}_e, y_m, y_{\mathrm{e}^-})$ in § 3.2. One can notice that f_{t-e,T_∞}^{neu} only depends on dimensional variable T_∞ like $f'_{Q_{e-v_m},T_\infty}$, whereas $f^{ion}_{t-e,T_\infty,\rho_\infty}$ not only depends on T_∞ but also is dependent on ρ_∞. Therefore, it is observed that the energy exchange between translation and electron mode caused by electron–ion collisions, Q_{t-e_ions}, can invalidate the binary scaling law. If the energy exchange caused by electron–ion collisions is small enough compared with electron–electronic energy change caused by other means, the binary scaling law will be approximately applicable.

Due to the preceding three-body reactions in the reverse reaction, the electron–electronic energy change resulting from chemical reactions (including $\sum_{s=1}^{ns}\omega_s E_{e_s}$, $I_{\mathrm{O}}\omega_{\mathrm{O}^+}$ and $I_{\mathrm{N}}\omega_{\mathrm{N}^+}$) can make the binary scaling law invalid. Similar to the analysis for term $(L/\rho_\infty U_\infty^3)\omega_m E_{v_m}$ in (3.11), the binary scaling law can be applied to the electron–electronic energy conservation equation if the incoming flow density ρ_∞ is sufficiently low.

The term $-(Lp_e/\rho_\infty U_\infty^3)(\partial u_j/\partial x_j)$ can be expressed as

$$-\frac{Lp_e}{\rho_\infty U_\infty^3}\frac{\partial u_j}{\partial x_j} = -\frac{T_\infty R_u y_{e^-}}{U_\infty^2 M_{e^-}}\frac{\bar{\rho}\bar{T}_e\partial\bar{u}_j}{\partial\bar{x}_j}. \tag{3.18}$$

One can observe from (3.18) that the term $-(Lp_e/\rho_\infty U_\infty^3)(\partial u_j/\partial x_j)$ only depends on dimensional parameters T_∞, U_∞ and does not affect the feasibility of the binary scaling law.

Thus, Q_{t-e}, Q_{r-e} and Q_{i-e} in the electron–electronic energy conservation equation are the terms that could potentially invalidate the binary scaling law. For Q_{r-e} and Q_{i-e}, the primary cause is still three-body reactions. For Q_{t-e}, the primary cause is the translation–electron energy exchange resulting from electron–ion collisions, Q_{t-e_ions}.

4. Numerical analysis

The governing equations with the multi-temperature model are discretized by cell-centred finite volume method based on unstructured scheme. The inviscid fluxes are calculated using a modified Harten–Lax–van Leer contact scheme (Kim *et al.* 2009) with second-order multi-dimensional limiting process (MLP) (Park, Yoon & Kim 2010) reconstruction and MLP pressure-weighted limiter (Zhang, Liu & Chen 2018). The second-order central difference scheme is applied for viscous flux calculation. The lower–upper symmetric Gauss–Seidel implicit algorithm (Blazek 2015) is employed for time integration. The Gupta and the Park chemical reaction models with 11-species and four-temperature model with vibrational temperature of N_2 and O_2 are employed.

In this section, all the meshes of different cases have high quality near the wall. The wall mesh Reynolds number based on local parameters next to the wall is defined as follows:

$$Re_{cell} = \frac{\rho_w c_w \Delta x}{\mu_w}, \tag{4.1}$$

where c is speed of sound and Δx denotes the normal height of the first grid at the wall. The subscript w denotes the parameters near the wall. The accuracy of heat flux calculation is guaranteed when the value of Re_{cell} is less than or equal to 3 (Men'shov & Nakamura 2000). In this paper, the maximum wall mesh Reynolds numbers $Re_{cell,max}$ of all the cases are located at their corresponding stagnation point and are less than 3.

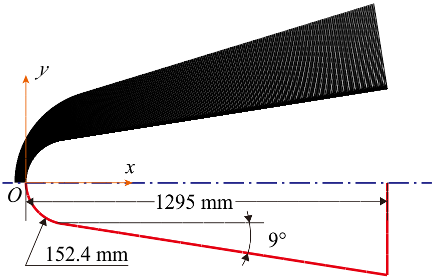

Figure 1. Geometry and grid of RAM-C II vehicle (top: grid; bottom: geometry of vehicle).

Grid		Free-stream condition				Wall	
N_{cell} (axial × radial)	$Re_{cell,max}$	h_∞ (km)	P_∞ (Pa)	T_∞ (K)	Ma_∞	T_w (K)	Boundary
212 × 109	0.14	71	4.7	215.79	25.9	1500	Isothermal, fully catalytic

Table 1. Computational conditions for RAM-C II vehicle.

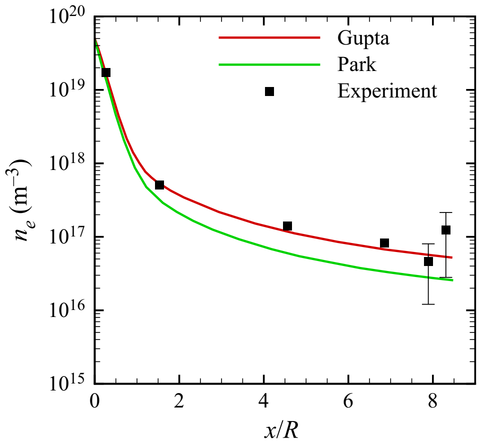

Figure 2. Peak electron number density along the surface of RAM-C II vehicle at 71 km.

4.1. *Code validation*

The flight experimental data of RAM-C II vehicle (Jones & Cross 1972) are used for code validation. The geometry of RAM-C II vehicle and grid of the computation field are illustrated in figure 1. The detailed computational conditions are listed in table 1.

A comparison of peak electron number density along the RAM-C II vehicle surface at 71 km between CFD predicted result and flight data is plotted in figure 2. It is observed that the distribution of maximum electron number densities calculated by the Gupta model presents a good agreement with the experimental data. Although the distribution of peak electron number density predicted by the Park model results in a poorer agreement with the flight data compared with that predicted by the Gupta model, the result obtained by the Park model is no more than an order of magnitude different from the experimental data on the whole and has the same trend as the experimental data.

Cylinder	Free-stream condition						Wall	
Radius R (m)	h_∞ (km)	ρ_∞ (kg m^{-3})	$\rho_\infty R$ (kg m^{-2})	P_∞ (Pa)	T_∞ (K)	Ma_∞	T_w (K)	Boundary
0.15	70	8.754×10^{-5}	1.3131×10^{-5}	5.52	219.7	27	1300	Isothermal, fully catalytic
0.015	–	8.754×10^{-4}	1.3131×10^{-5}	55.2	219.7	27	1300	Isothermal, fully catalytic

Table 2. Computational conditions for original ($R = 0.15$ m) and 10-times-scaled ($R = 0.015$ m) cylinders.

Cylinder	Grid	N_{cell} (circumferential × radial)	$Re_{cell,max}$
$R = 0.15$ m	A	131 × 84	0.21
	B	191 × 144	0.21
	C	221 × 174	0.21
$R = 0.015$ m	A	131 × 84	2.1
	B	191 × 144	2.1
	C	221 × 174	2.1

Table 3. Mesh information for cylinders at $Ma_\infty = 27$ with $\rho_\infty R = 1.3131 \times 10^{-5}$ kg m^{-2}.

4.2. *The failure of the binary scaling law for electron distribution*

The applicability of the binary scaling similarity law for thermochemical non-equilibrium air was examined using the classical case of flow around cylinders. The original cylinder which had a radius of 0.15 m and its 10-times-smaller model were used for numerical simulation. The original cylinder was subjected to a free-stream condition of 70 km and Mach 27 while the scaled-down cylinder had its free-stream density magnified 10 times to ensure that the condition of the binary scaling law ($\rho_\infty R = \text{const.}$) is satisfied. The detailed computational conditions are listed in table 2.

Grid independence studies of the original and scaled-down cylinders were implemented with three different grids: A, B and C. The grid quality increases from A to C by increasing both the circumferential and radial grid numbers. Detailed information of the grids is given in table 3. Grids A, B and C are constructed with the same normal size of the first cell next to surfaces. All the meshes are refined near the bow shock and Grid B with medium quality for two cylinders is illustrated in figure 3. The distributions of electron number density along the stagnation line for both the original and the scaled-down cylinders using Grids A, B and C are shown in figure 4. The results with different grid resolutions apparently demonstrate good agreement. According to the results with Grids B and C, the flow parameters no longer rely on the quality of the grid. Therefore, only the results calculated with Grid B are used for the later analysis.

Figure 5 shows the Mach number and e$^-$ mass fraction contours of the original and scaled cylinders at $Ma_\infty = 27$ using the Gupta model. Although there is a good similarity in the bow-shock shape between the two cylinders, the distributions of free electrons are significantly different between the two cylinders. Figure 6 shows the distributions of T, T_e, T_{vN_2} and T_{vO_2} along the stagnation streamline at $Ma_\infty = 27$ using the Gupta model. It is observed that the temperatures of the two flows maintain a good similarity on the whole despite the relatively small differences in local regions. The mass fractions of free electrons and ions along the stagnation line are plotted in figure 7. As shown figure 7(*a*,*b*),

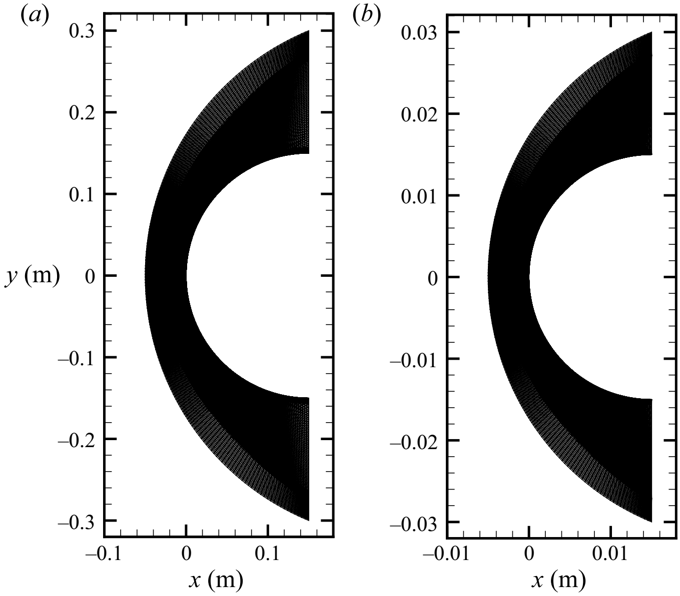

Figure 3. Grid B of cylinders at 70 km and $Ma_\infty = 27$. (*a*) Original cylinder of $R = 0.15$ m. (*b*) Scaled cylinder of $R = 0.015$ m.

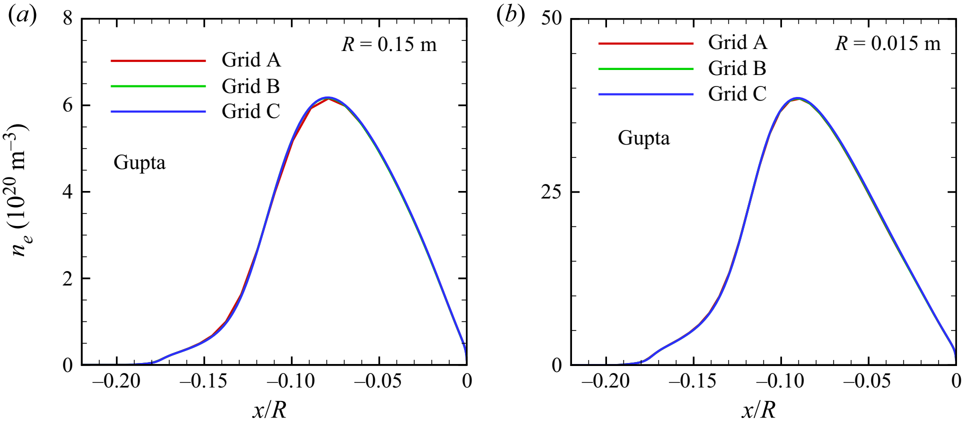

Figure 4. Comparisons of distributions of electron number density along the stagnation line using different grids at $Ma_\infty = 27$ with the Gupta model. (*a*) Original cylinder. (*b*) Scaled cylinder.

the gaps of maximum mass fraction between original and scaled cylinders for N^+, NO^+ and N_2^+ are all no more than 6 %. Nevertheless, figure 7(*c*,*d*) indicates that there are tremendous differences between the original and scaled cylinders for mass fractions of e^- and O^+. The difference in peak mass fraction on the stagnation line between the two cylinders reaches 50.4 % for e^- and 59.0 % for O^+. As such, the binary scaling law fails completely for distribution of e^- at $Ma_\infty = 27$ with the Gupta model.

Figure 8 shows the distributions of e^-, O^+ and temperatures along the stagnation line at $Ma_\infty = 27$ using the Park model. It is observed that the binary scaling law holds well for the distributions of e^- and O^+ when the Park model is employed. Furthermore, the

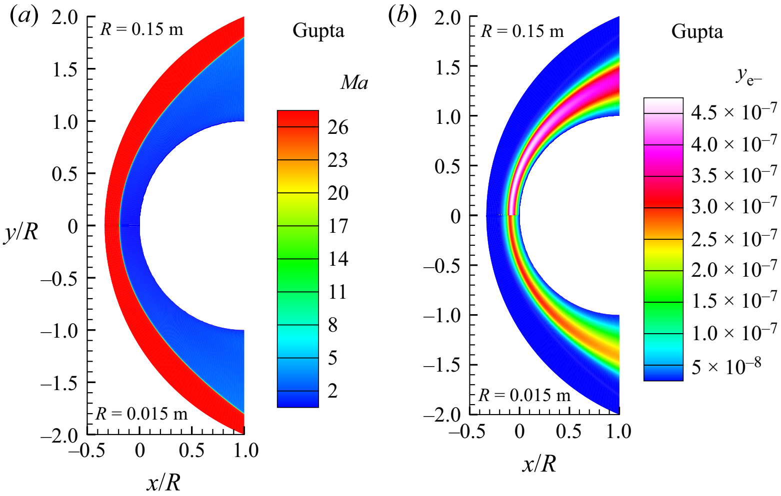

Figure 5. Contours of (*a*) Mach number and (*b*) mass fraction of e^- at $Ma_\infty = 27$ with $\rho_\infty R = 1.3131 \times 10^{-5}$ kg m^{-2} using the Gupta model (top: original cylinder; bottom: scaled cylinder).

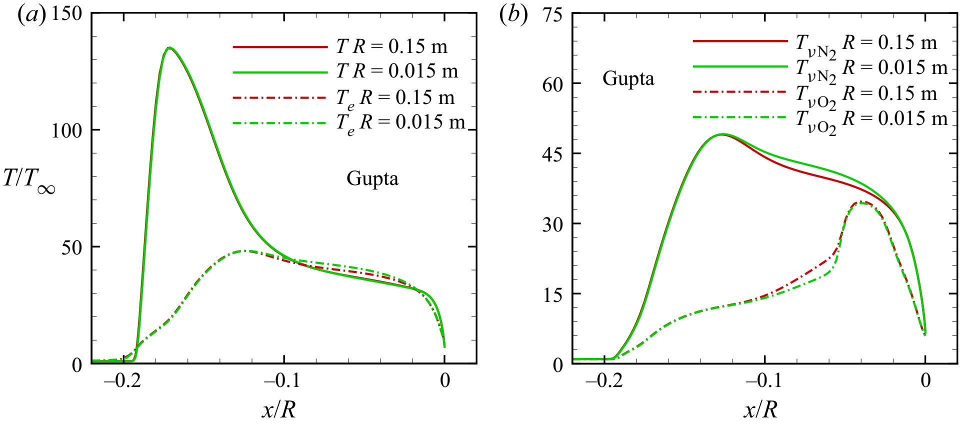

Figure 6. Distributions of temperatures along the stagnation line at $Ma_\infty = 27$ with $\rho_\infty R = 1.3131 \times 10^{-5}$ kg m^{-2} using the Gupta model. (*a*) Translational–rotational and electron–electronic temperatures and (*b*) N_2 and O_2 vibrational temperatures.

similarity in temperatures between the two cylinders using the Park model is greater than that using the Gupta model. However, the binary scaling law was found to be invalid for modelling electron distribution using the Park model when Ma_∞ increases to 39 (other boundary conditions remain unchanged). The distributions of e^- and N^+ at $Ma_\infty = 39$ using the Park model are illustrated in figure 9 (the detailed information of grids is listed in table 4). It is observed that the peak mass fraction of e^- and N^+ in the original cylinder is obviously higher that in the scaled-down cylinder at $Ma_\infty = 39$ using the Park model. Zeng *et al.* (2009) also found that, at $\rho_\infty R = 1.3131 \times 10^{-5}$ and $U_\infty = 7650$ m s^{-1}, the binary scaling law failed for distribution of O^+ by numerical simulation of RAM-C II and its scaled model using the Gupta model.

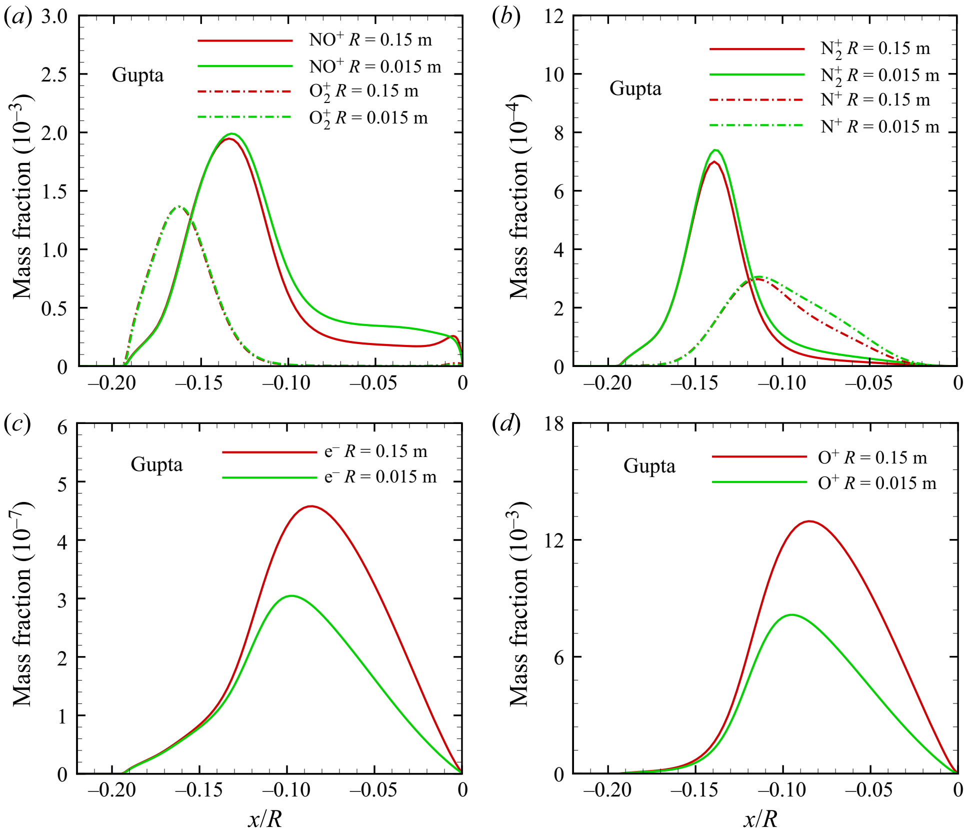

Figure 7. Distributions of electrons and ions along the stagnation line at $Ma_\infty = 27$ with $\rho_\infty R = 1.3131 \times 10^{-5}$ kg m^{-2} using the Gupta model. Mass fractions of (*a*) NO^+ and O_2^+, (*b*) N_2^+ and N^+, (*c*) e^- and (*d*) O^+.

Cylinder	N_{cell} (circumferential × radial)	$Re_{cell,max}$
$R = 0.15$ m	191 × 144	0.21
$R = 0.015$ m	191 × 144	2.1

Table 4. Mesh information for cylinders at $Ma_\infty = 39$ with $\rho_\infty R = 1.3131 \times 10^{-5}$ kg m^{-2}.

4.3. *Effect of the electron-impact ionization reactions*

According to the analysis in § 3.1, the three-body reaction is one of the main reasons for the invalidation of the binary scaling law. We try to find out which three-body reactions caused the failure of the binary scaling law for the electron distribution at high altitude with extremely high Mach number. The formation of free electrons is governed by seven elementary reactions in the Gupta air-chemistry model: (i) associative ionization reactions ($N + O \rightleftharpoons NO^+ + e^-$, $O + O \rightleftharpoons O_2^+ + e^-$ and $N + N \rightleftharpoons N_2^+ + e^-$), (ii) electron-impact ionization reactions ($O + e^- \rightleftharpoons O^+ + e^- + e^-$ and $N + e^- \rightleftharpoons N^+ + e^- + e^-$) and (iii) other reactions ($O_2 + N_2 \rightleftharpoons NO^+ + NO + e^-$ and $NO + M \rightleftharpoons NO^+ + e^- + M$). Noticing that the shape of the distribution curve of e^- is very

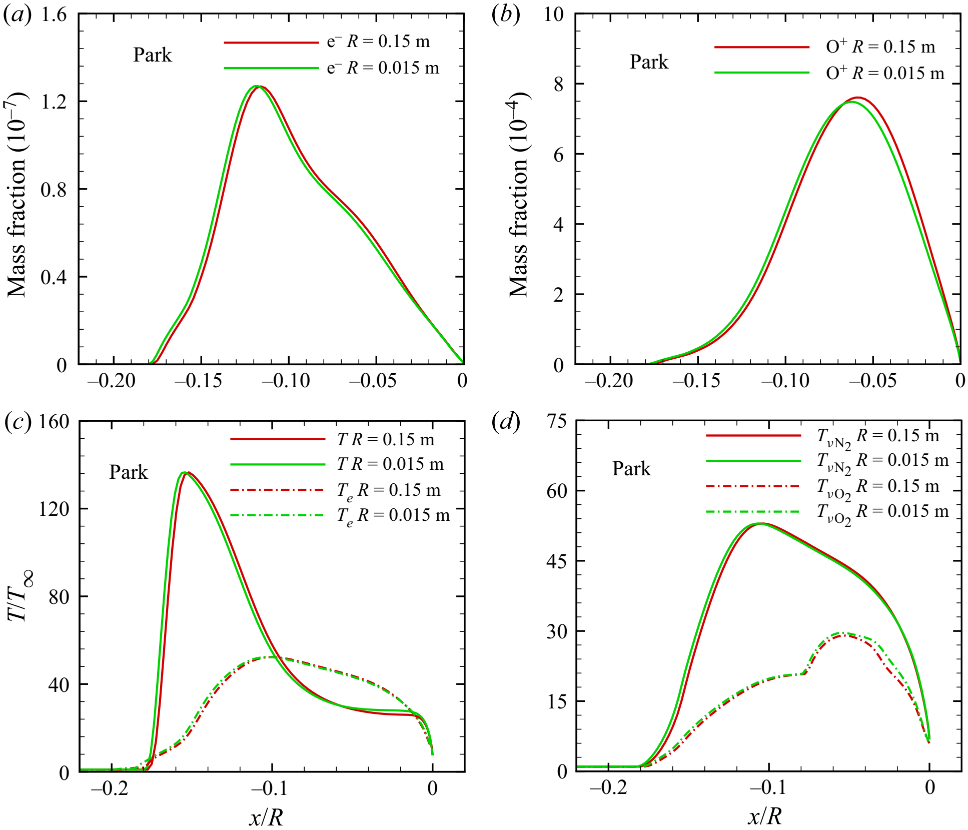

Figure 8. Distributions of e^-, O^+ and temperatures along the stagnation line at $Ma_\infty = 27$ with $\rho_\infty R = 1.3131 \times 10^{-5}$ kg m^{-2} using the Park model. Mass fractions of (*a*) e^- and (*b*) O^+. (*c*) Translational–rotational and electron–electronic temperatures and (*d*) N_2 and O_2 vibrational temperatures.

similar to that of O^+ from figure 7(*c*,*d*), it is speculated that the dissimilarity of electron distribution might be related to $O + e^- \rightleftharpoons O^+ + e^- + e^-$ in the Gupta model. The dimensionless reaction rates can be defined as follows:

$$\overline{R_z^{fb}}, \overline{R_z^{f}}, \overline{R_z^{b}} = \frac{R_z^{fb}, R_z^{f}, R_z^{b}}{\rho_\infty U_\infty/(RM_{mix,\infty})}, \tag{4.2}$$

where $M_{mix,\infty}$ is the average molar mass of free stream and R is the radius of the cylinder. The dimensionless total reaction rates of the foregoing seven elementary reactions are plotted in figure 10. It is obvious that the reaction $O + e^- \rightleftharpoons O^+ + e^- + e^-$ plays the most dominant role in formation of free electrons. Figure 11 shows the dimensionless reaction rate of $O + e^- \rightleftharpoons O^+ + e^- + e^-$ on the stagnation line. As shown in figure 11(*a*), the dimensionless total reaction rates of $O + e^- \rightleftharpoons O^+ + e^- + e^-$ for the original and scaled models are dissimilar and the difference of maximum reaction rates between the two reaches 26.3 %. As described in § 3.1, the precondition for the binary scaling law is that the two-body forward reaction rate is far larger than the three-body backward reaction rate, whereas both the original and scaled cylinders demonstrate a backward reaction rate of $O + e^- \rightleftharpoons O^+ + e^- + e^-$ of the same order of magnitude as the forward reaction rate, as illustrated in figure 11(*b*).

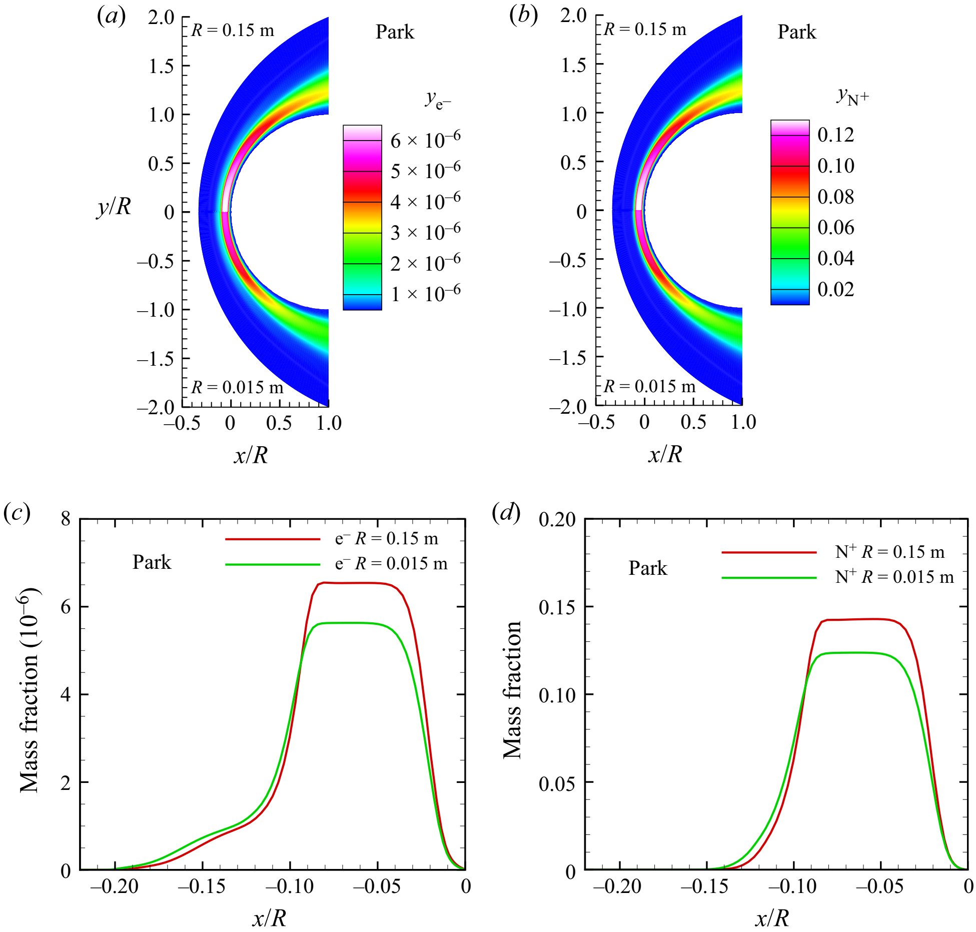

Figure 9. Distributions of e^- and N^+ at $Ma_\infty = 39$ with $\rho_\infty R = 1.3131 \times 10^{-5}$ kg m^{-2} using the Park model. (*a*) Contours of mass fraction of e^-, (*b*) contours of mass fraction of N^+, (*c*) mass fraction of e^- along the stagnation line and (*d*) mass fraction of N^+ along the stagnation line.

In light of the fact that the binary scaling law did not fail at $Ma_\infty = 27$ using the Park model, reaction rate coefficients of $O + e^- \rightleftharpoons O^+ + e^- + e^-$ in the Gupta model were replaced with those in the Park model to verify the preceding assumption. Leaving the computational conditions listed in table 2 unchanged, the Gupta model was still adopted for coefficients of other reactions and the results are illustrated in figure 12. It can be observed that the binary scaling law works well for distributions of electrons, ions and temperatures. As a consequence, it can be inferred that the electron-impact ionization reaction $O + e^- \rightleftharpoons O^+ + e^- + e^-$ is the main reason causing the dissimilarity in flow field using the Gupta model.

Figure 13 compares the dimensionless reaction rate of $O + e^- \rightleftharpoons O^+ + e^- + e^-$ along the stagnation streamline between the two cylinders with only reaction rate coefficients of $O + e^- \rightleftharpoons O^+ + e^- + e^-$ calculated using the Park model. Although there are obvious differences between the two cylinders for the three-body reverse reaction rate of $O + e^- \rightleftharpoons O^+ + e^- + e^-$ from figure 13(*a*), the two-body forward reaction rates of that between the two cylinders have good similarity and the three-body reverse reaction rate can be

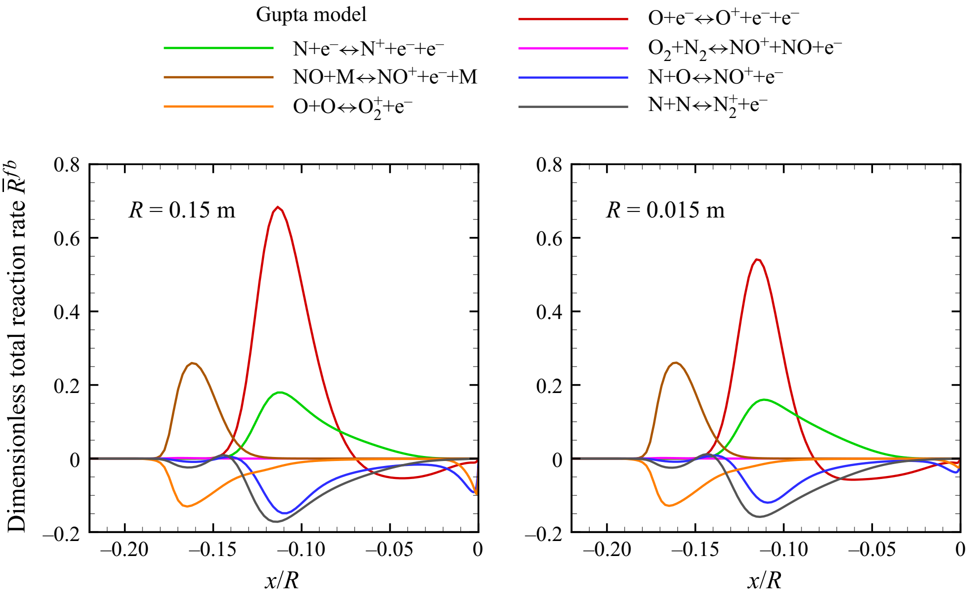

Figure 10. The dimensionless total rates of reactions related to generation of e^- along the stagnation line at $Ma_\infty = 27$ with $\rho_\infty R = 1.3131 \times 10^{-5}$ kg m^{-2} using the Gupta model.

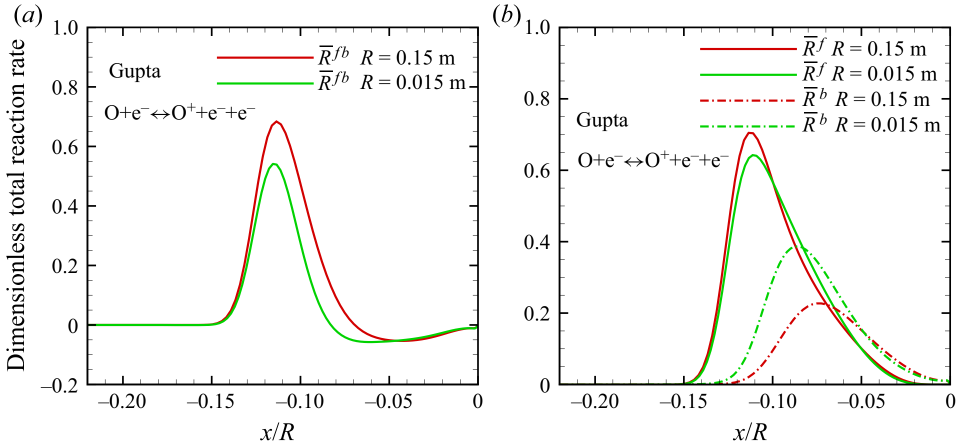

Figure 11. The dimensionless reaction rate of $O + e^- \rightleftharpoons O^+ + e^- + e^-$ along the stagnation line at $Ma_\infty = 27$ with $\rho_\infty R = 1.3131 \times 10^{-5}$ kg m^{-2} using the Gupta model. (*a*) Total reaction rate. (*b*) Forward and backward reaction rate.

negligible compared to the forward reaction rate from figure 13(*b*). Thus, $O + e^- \rightleftharpoons O^+ + e^- + e^-$ satisfies the necessary conditions of the binary scaling law in this case.

The ratio of the forward reaction rate of $O + e^- \rightleftharpoons O^+ + e^- + e^-$ to the reverse reaction rate γ_{O+e^-} is defined as follows:

$$\gamma_{O+e^-} = \frac{\frac{\rho_O}{M_O}\frac{\rho_{e^-}}{M_{e^-}}k^f_{O+e^-}(T_e)}{\frac{\rho_{O^+}}{M_{O^+}}\frac{\rho_{e^-}}{M_{e^-}}\frac{\rho_{e^-}}{M_{e^-}}k^b_{O+e^-}(T_e)} = \frac{M_{O^+}M_{e^-}}{M_O\rho}\frac{y_O}{y_{O^+}y_{e^-}}K_{eq,O+e^-}(T_e). \qquad (4.3)$$

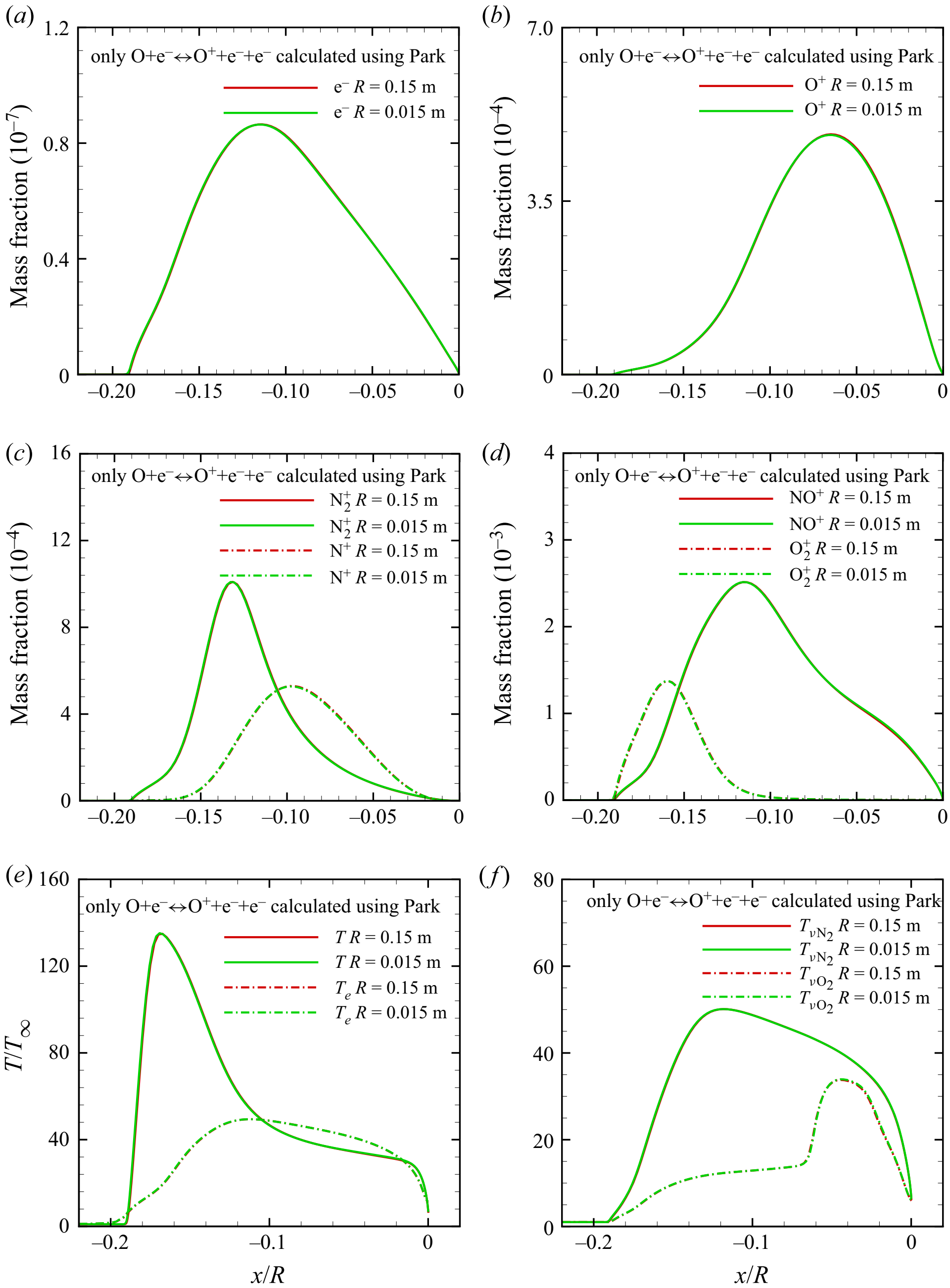

Figure 12. Distributions of electrons, ions and temperatures along the stagnation line at $Ma_\infty = 27$ with only the reaction rate of $O + e^- \rightleftharpoons O^+ + e^- + e^-$ calculated using the Park model (the Gupta model is employed for other reactions). (*a*) Mass fraction of e^-, (*b*) mass fraction of O^+, (*c*) mass fraction of N_2^+ and N^+, (*d*) mass fraction of NO^+ and O_2^+, (*e*) translational–rotational and electron–electronic temperatures and (*f*) N_2 and O_2 vibrational temperatures.

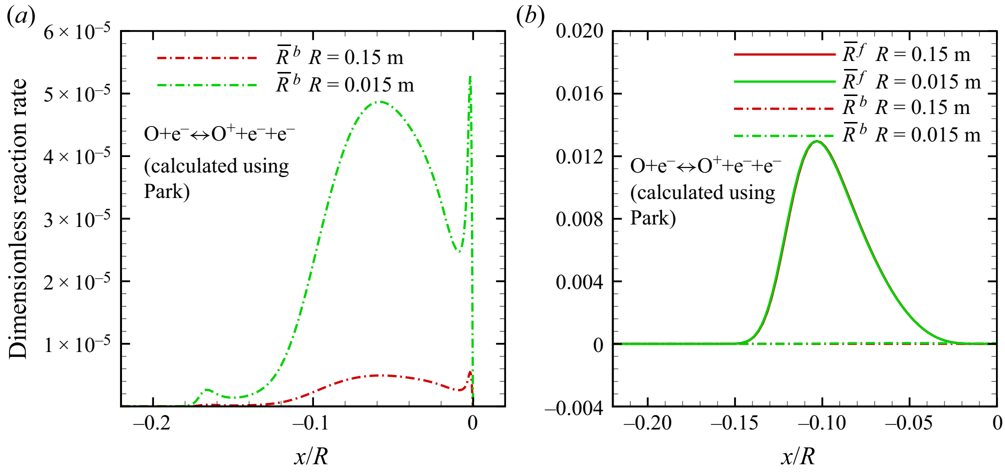

Figure 13. The dimensionless reaction rate of $O + e^- \rightleftharpoons O^+ + e^- + e^-$ along the stagnation line at $Ma_\infty = 27$ with only reaction rate coefficients of $O + e^- \rightleftharpoons O^+ + e^- + e^-$ calculated using the Park model (the Gupta model is employed for other reactions). (*a*) Backward reaction rate. (*b*) Forward and backward reaction rate.

The reverse reaction rate of $O + e^- \rightleftharpoons O^+ + e^- + e^-$ calculated by the Gupta model is of the same order of magnitude as the forward reaction rate ($\gamma_{O+e^-} \sim 1$) and the precondition for the binary scaling law ($\gamma_{O+e^-} \gg 1$) is no longer satisfied. Here T_e is the controlling temperature of the forward and backward reaction rates for the electron-impact ionization reactions. At $Ma_\infty = 27$, the maximum T_e in cases using the Gupta model or the Park model for $O + e^- \rightleftharpoons O^+ + e^- + e^-$ are close from figures 6(*a*) and 12(*e*). One can notice that the equilibrium constant of $O + e^- \rightleftharpoons O^+ + e^- + e^-$ in the Gupta model is close to that in the Park model from figure 14(*a*). Combined with (4.3), figures 7(*c*,*d*) and 12(*a*,*b*), it can be seen that higher mass fraction of O^+ and e^- is the reason that γ_{O+e^-} with the Gupta model is far less than that with the Park model. Figure 14(*b*) compares the forward reaction rate coefficient of $O + e^- \rightleftharpoons O^+ + e^- + e^-$ from Gupta and Park models as a function of the controlling temperature according to (2.14*a*,*b*). It is clear that the forward reaction rate coefficient of the Gupta model is more than one order of magnitude larger than that of the Park model at the corresponding peak T_e. Higher forward reaction rate with the Gupta model caused the reaction to move in the positive direction and produce more O^+ and e^-, which increased the backward reaction rate and reduced γ_{O+e^-} to around 1.

The formation of free electrons is governed by five elementary reactions in the Park model: (i) associative ionization reactions ($N + O \rightleftharpoons NO^+ + e^-$, $O + O \rightleftharpoons O_2^+ + e^-$ and $N + N \rightleftharpoons N_2^+ + e^-$) and (ii) electron-impact ionization reactions ($O + e^- \rightleftharpoons O^+ + e^- + e^-$ and $N + e^- \rightleftharpoons N^+ + e^- + e^-$). The dimensionless total reaction rates of these five elementary reactions along the stagnation line at $Ma_\infty = 39$ using the Park model are depicted in figure 15. It can be seen that the electron-impact ionization reaction $N + e^- \rightleftharpoons N^+ + e^- + e^-$ is dominant in the formation of e^-. The other electron-impact ionization reaction $O + e^- \rightleftharpoons O^+ + e^- + e^-$ also plays an important role in electron formation near the location where a significant difference in electron mass fraction began to appear ($x/R = -0.09$; see figure 9*c*). Figure 16 shows the dimensionless reaction rates of the two electron-impact ionization reactions along the stagnation streamline at $Ma_\infty = 39$ using the Park model. It is noticed that the backward reaction rate is of the same order

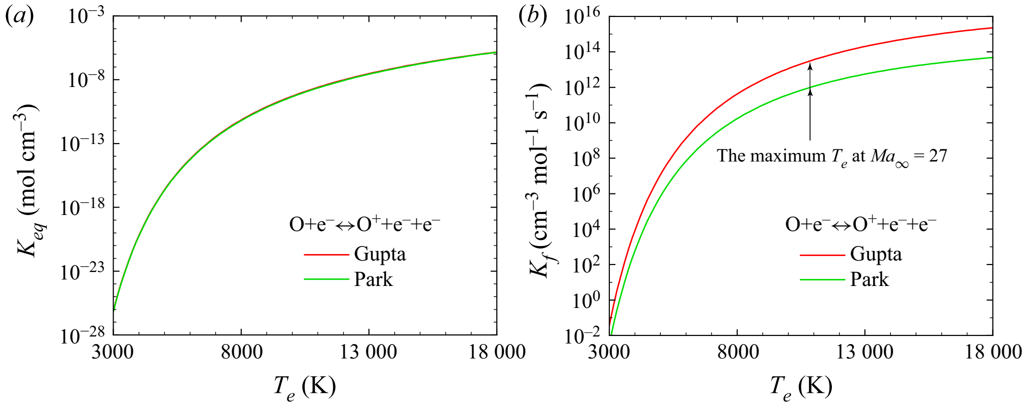

Figure 14. The equilibrium constants and forward reaction rate coefficients of $O + e^- \rightleftharpoons O^+ + e^- + e^-$ in the Gupta and Park models. (*a*) Equilibrium constants (particle number density equals 1.0×10^{15} cm^3 in the Park model). (*b*) Forward reaction rate coefficients (the arrows represent the maximum electron–electronic excitation temperatures in figures 6*a* and 12*e*).

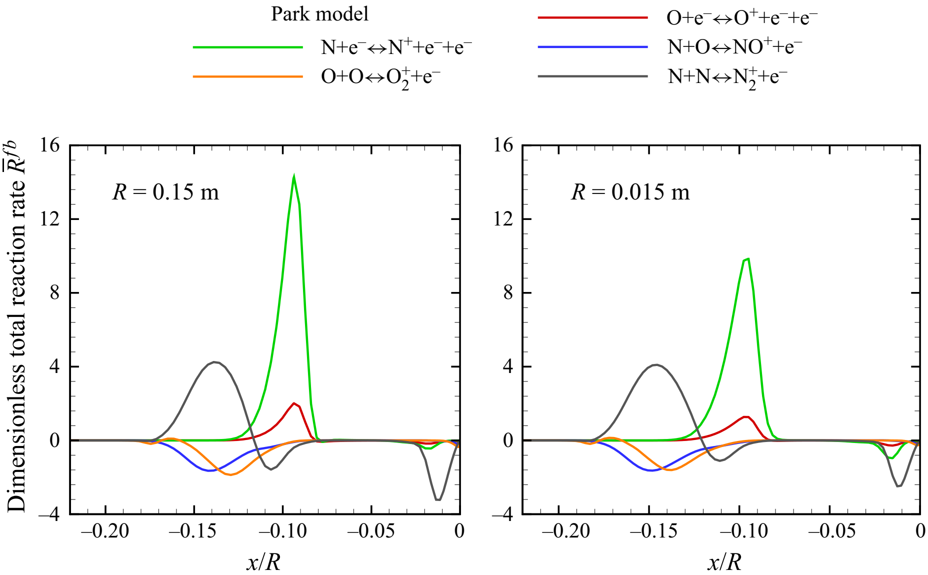

Figure 15. The dimensionless total rates of reactions related to generation of e^- along the stagnation line at $Ma_\infty = 39$ using the Park model.

of magnitude as the forward reaction rate for both reactions, which leads to the significant differences in total reaction rate between the original and scaled cylinders in figure 16(*b*,*d*).

Figure 17 compares the forward reaction rate coefficient of two electron-impact ionization reactions in the Gupta and Park models. Considering the foregoing results at $Ma_\infty = 27$ and 39 with the Gupta and Park models, one can see that the binary scaling law is invalid for electron distribution when the forward reaction rate coefficient k^f of electron-impact ionization reactions rises to a certain degree with an increase of Ma_∞. In order to further verify this, Ma_∞ is reduced to 17 (other boundary conditions remain unchanged and the detailed information of grids is listed in table 5). Figure 18 shows the

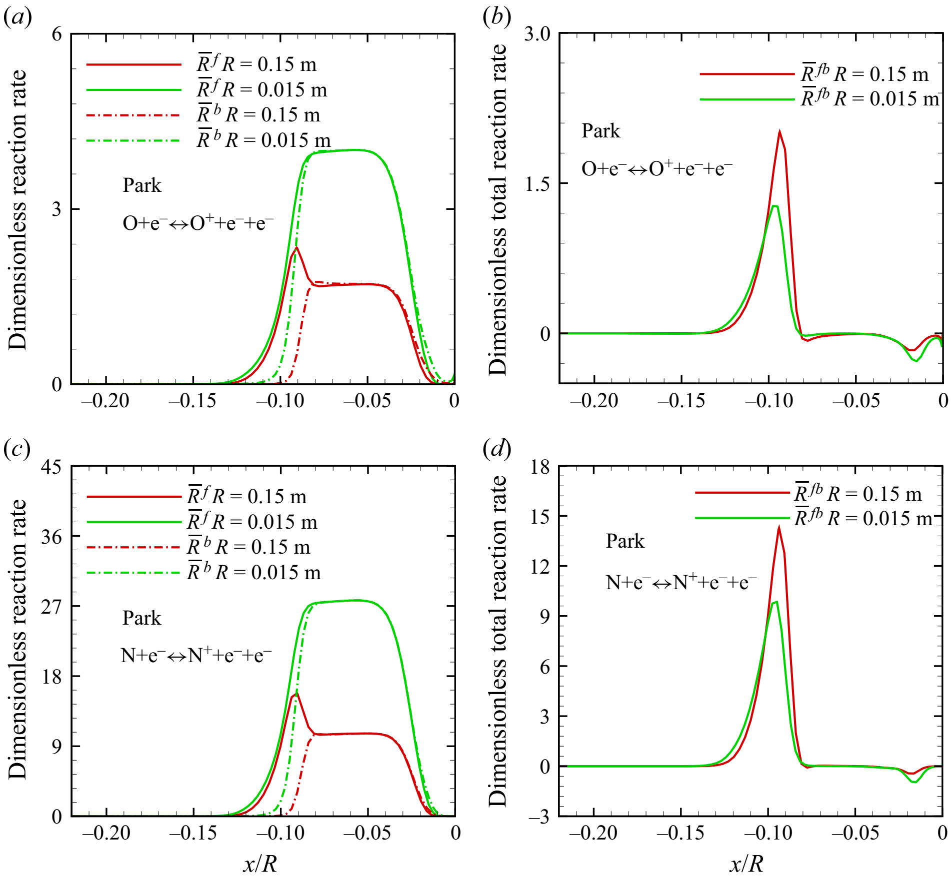

Figure 16. The dimensionless reaction rate of two electron-impact ionization reactions along the stagnation line at $Ma_\infty = 39$ using the Park model. (*a*) Forward and backward reaction rate of $\mathrm{O + e^- \rightleftharpoons O^+ + e^- + e^-}$. (*b*) Total reaction rate of $\mathrm{O + e^- \rightleftharpoons O^+ + e^- + e^-}$. (*c*) Forward and backward reaction rate of $\mathrm{N + e^- \rightleftharpoons N^+ + e^- + e^-}$. (*d*) Total reaction rate of $\mathrm{N + e^- \rightleftharpoons N^+ + e^- + e^-}$.

Cylinder	N_{cell} (circumferential × radial)	$Re_{cell,max}$
$R = 0.15$ m	191 × 144	0.19
$R = 0.015$ m	191 × 144	1.9

Table 5. Mesh information for cylinders at $\rho_\infty R = 1.3131 \times 10^{-5}$ kg m^{-2} with $Ma_\infty = 17$.

distributions of $\mathrm{e^-}$ and $\mathrm{O^+}$ along the stagnation line at $Ma_\infty = 17$ using the Gupta model. One can observe that there is good agreement in the distributions of $\mathrm{e^-}$ and $\mathrm{O^+}$ between the original and scaled cylinders (see figure 18) with a decrease in k^f of electron-impact ionization reactions at $Ma_\infty = 17$ using the Gupta model (see figure 17).

Due to effects of the electron avalanche, it is hard to measure the forward reaction rates of electron-impact ionization reactions (Park 1990; Hao *et al.* 2016). However, the reverse reactions of electron-impact ionization are very nearly in quasi-steady-state distribution and the forward reaction rates can be calculated using the reverse reaction rates and

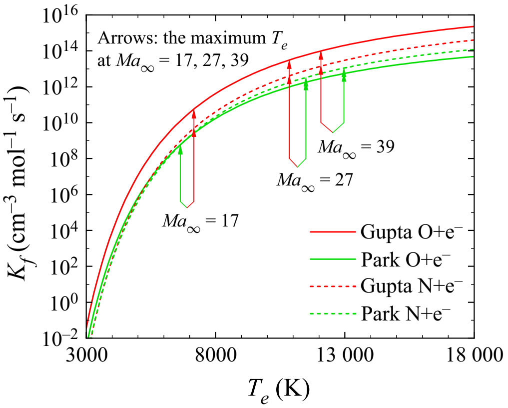

Figure 17. Forward reaction rate coefficient of two electron-impact ionization reactions in the Gupta and Park models (the red arrow represents the maximum electron temperature of the flow field around the cylinder under the corresponding Ma_∞ using the Gupta model and the green arrow represents that using the Park model).

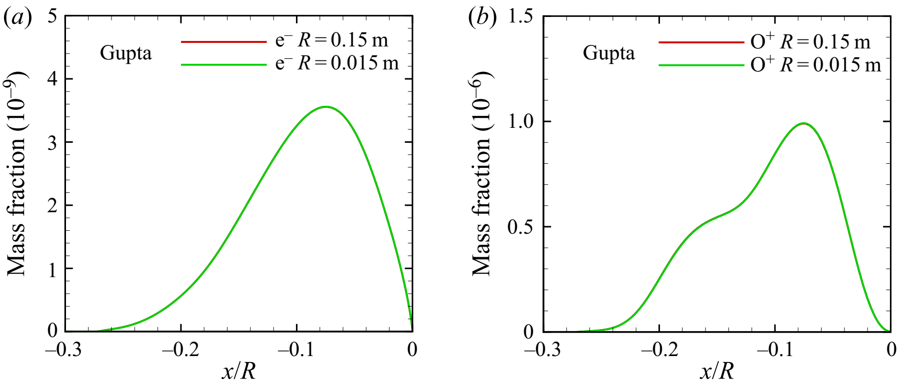

Figure 18. Distributions of e^- and O^+ along the stagnation line at $Ma_\infty = 17$ with $\rho_\infty R = 1.3131 \times 10^{-5}$ kg m^{-2} using the Gupta model. Mass fractions of (*a*) e^- and (*b*) O^+.

equilibrium constants (Park 1990). Park measured the ionic recombination rate of N atom $N^+ + e^- + e^- \rightarrow N + e^-$ by observing the rate of decrease of electron density in an expanding nozzle (Park 1990, 1968, 1973). Although the rates of $O^+ + e^- + e^- \rightarrow O + e^-$ have never been measured, the ionic recombination rate coefficients of various atoms (such as C, Ar, He) are fairly similar (Park 1990). Thus, Park assumed the recombination rates of O^+ to be the same as that of N^+ and obtained the rate coefficient of $O + e^- \rightleftharpoons O^+ + e^- + e^-$. This assumption is also embodied in the Gupta model. The rate coefficients of electron-impact ionization reactions in the Gupta model are taken from the model of Dunn and Kang (Dunn & Kang 1973; Gupta *et al.* 1990). Only the three-body ionic recombination rate coefficient for $C^+ + e^- + e^- \rightarrow C + e^-$ was measured by Dunn (1971). Hao *et al.* (2016) found an abnormal non-equilibrium relaxation process in the FIRE II case at $Ma_\infty = 39$ simulated using the Gupta model, which proved to be a consequence of electron-impact ionization reaction rates calculated using the Gupta model. The problem was solved using modified coefficients of electron-impact ionization reactions based on the Park model. Hao considered that parameters for electron-impact

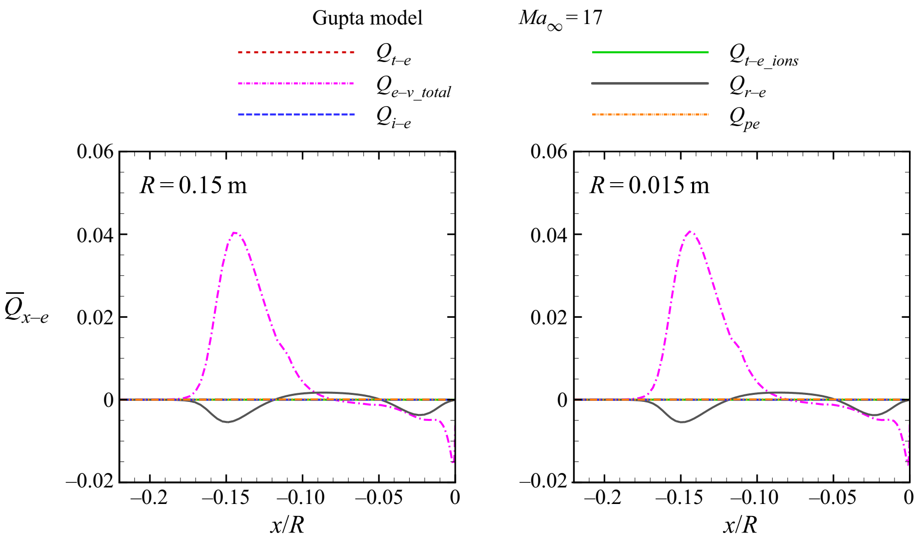

Figure 19. Dimensionless energy exchange between electrons and other mode along the stagnation line at $Ma_\infty = 17$ with $\rho_\infty R = 1.3131 \times 10^{-5}$ kg m^{-2} using the Gupta model.

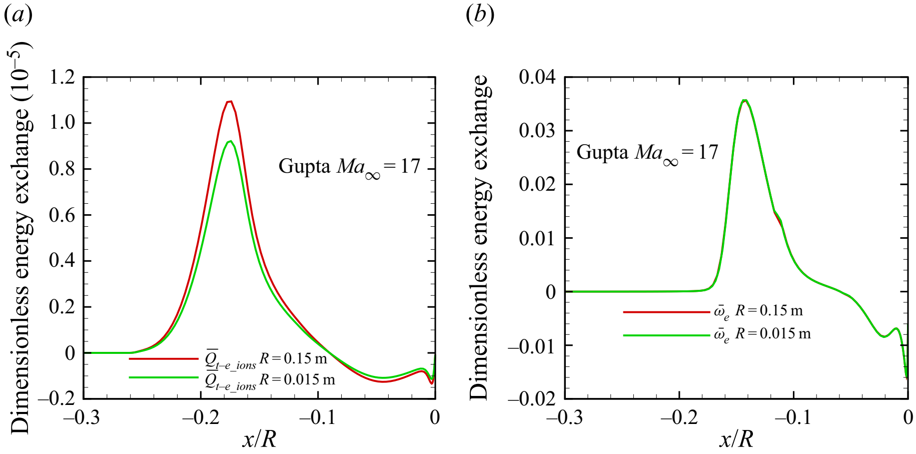

Figure 20. Dimensionless energy exchange (*a*) $\bar{Q}_{t-e\_ions}$ and (*b*) $\bar{\omega}_e$ along the stagnation line at $Ma_\infty = 17$ with $\rho_\infty R = 1.3131 \times 10^{-5}$ kg m^{-2} using the Gupta model.

ionization reactions in the Park model might be more accurate because Park's data were taken from more recent experiments. In addition, a more recent chemical kinetic model was developed by Ozawa, Zhong & Levin (2008) and the forward rate coefficient of $\mathrm{O} + \mathrm{e}^- \rightleftharpoons \mathrm{O}^+ + \mathrm{e}^- + \mathrm{e}^-$ at high temperature calculated using the Ozawa model is closer to that calculated using the Park model (Niu *et al.* 2018). Although the Gupta and Park models have their own advantages in predictions of species formations (Niu *et al.* 2018), based on the points discussed above, the result at $Ma_\infty = 27$ obtained using the Park model might be more reliable. The rates of electron-impact ionization reactions require to be further studied experimentally and theoretically because they strongly affect the applicable range of the binary scaling law for modelling electron distribution.

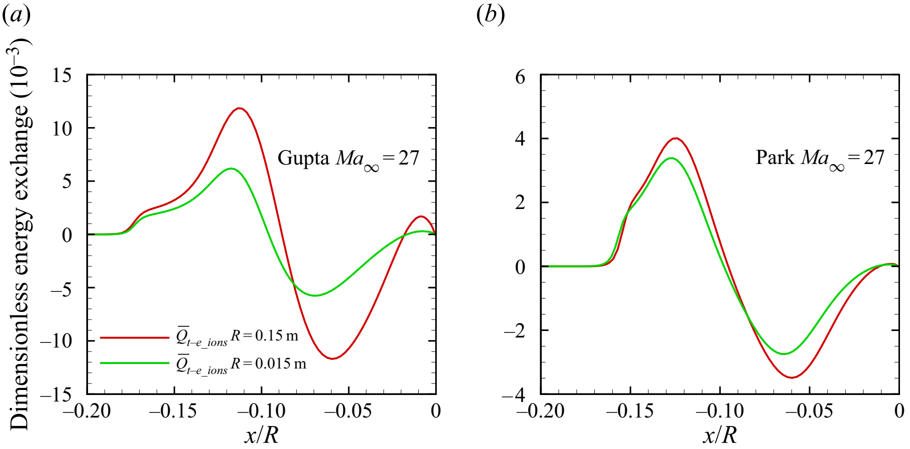

Figure 21. Dimensionless energy exchange $\bar{Q}_{t-e\_ions}$ along the stagnation line at $Ma_\infty = 27$ with $\rho_\infty R = 1.3131 \times 10^{-5}$ kg m^{-2}. (*a*) Gupta model. (*b*) Park model.

Although the differences in forward electron-impact ionization reaction rates between the Gupta and Park models can reach as much as an order of magnitude or more (Niu *et al.* 2018), the electron-impact ionization reactions can lead to the failure of the binary scaling law in electron distribution at extremely high Mach number no matter what chemical model is employed, which reflects that it is probably a general conclusion in nature.

4.4. *Discussion of electron–ion collisions*

In § 3.3, it is found that the translation–electron energy exchange from collisions between electrons and ions Q_{t-e_ions} can theoretically cause the failure of the binary scaling law. The dimensionless energy exchange source term can be defined as follows:

$$\overline{Q_x} = \frac{Q_x}{\rho_\infty {U_\infty}^3/R}, \tag{4.4}$$

where Q_x represents a certain energy exchange term in the vibrational or electron–electronic energy conservation equation and R is the radius of cylinder.

The dimensionless constituents of electron–electronic energy source term ω_e at $Ma_\infty = 17$ with the Gupta model are depicted in figure 19. It is noticed that Q_{t-e_ions} is so low relative to the dominant terms (Q_{e-v_total}, Q_{i-e}) that Q_{t-e_ions} can be ignored at $Ma_\infty = 17$. In figure 20(*a*), $\bar{Q}_{t-e\_ions}$ of the original cylinder is dissimilar to that of the scaled cylinder, which is consistent with theoretical analysis. Nevertheless, $\bar{\omega}_e$ of two cylinders still have good similarity from figure 20(*b*) because the contribution of $\bar{Q}_{t-e\_ions}$ is negligible.

Figure 21 shows the dissimilarity property of Q_{t-e_ions} at $Ma_\infty = 27$. Similar to the situation at $Ma_\infty = 17$, Q_{t-e_ions} is still too small to affect the total source term ω_e from figure 22.

As the number of ions and electrons increases at $Ma_\infty = 39$, it can be found from figure 23 that Q_{t-e_ions} and Q_{i-e} play the dominant role in the electron–electronic energy source term. Figure 24(*a*) shows the obvious dissimilarity of Q_{t-e_ions} and Q_{i-e} between the two cylinders at $Ma_\infty = 39$. It is clear that the trend of Q_{t-e_ions} is opposite to that of Q_{i-e} and the negative effects of the two on the similarity of the source term can be offset

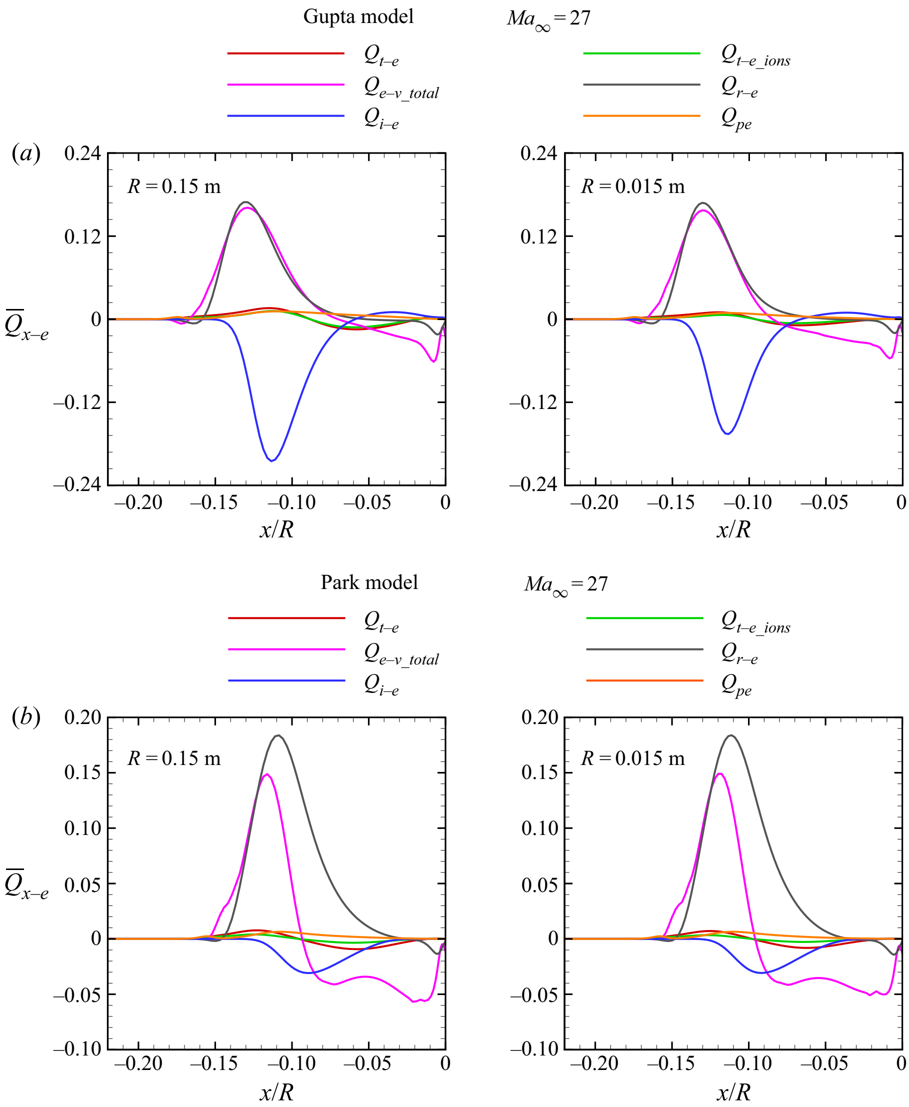

Figure 22. Dimensionless energy exchange between electrons and other mode along the stagnation line at $Ma_\infty = 27$ with $\rho_\infty R = 1.3131 \times 10^{-5}$ kg m^{-2}. (*a*) Gupta model. (*b*) Park model.

in part to some extent. The effect of dissimilarity of electron–electronic energy source term is directly embodied by the electron–electronic temperature T_e. In figure 24(*b*), there are relatively large differences in electron temperature between the two cylinders at some regions. This means that the influence of Q_{t-e_ions} on the binary scaling law cannot be neglected at extremely high Mach number. Temperature T_e is the controlling temperature of some reactions (for example, the electron-impact ionization reactions), which affects the formation of electrons and ions and the production of electrons and ions is directly related to Q_{t-e_ions}. As a result, Q_{t-e_ions} and production of e$^-$ are coupled, which means that the quantification of the effect on the dissimilarity of electron distribution caused by Q_{t-e_ions} is complicated.

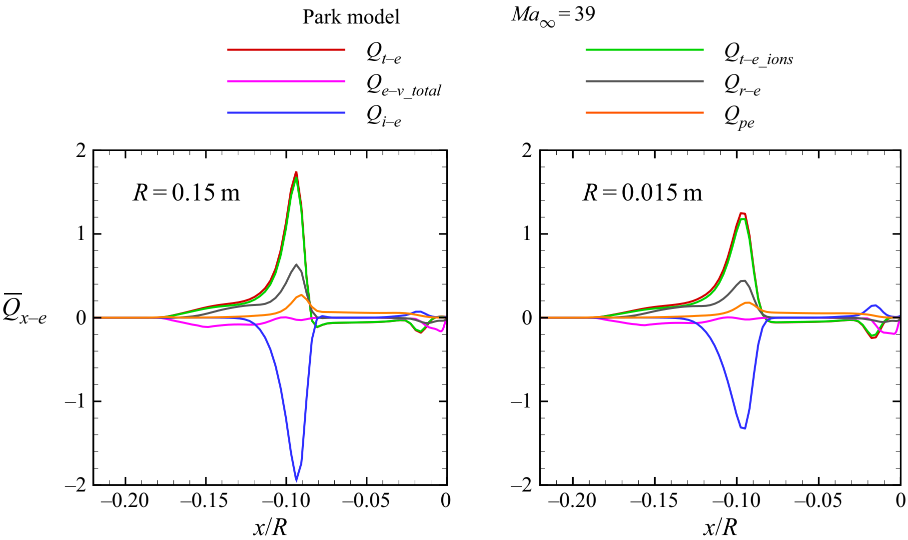

Figure 23. Dimensionless energy exchange between electrons and other mode along the stagnation line at $Ma_\infty = 39$ with $\rho_\infty R = 1.3131 \times 10^{-5}$ kg m^{-2} using the Park model.

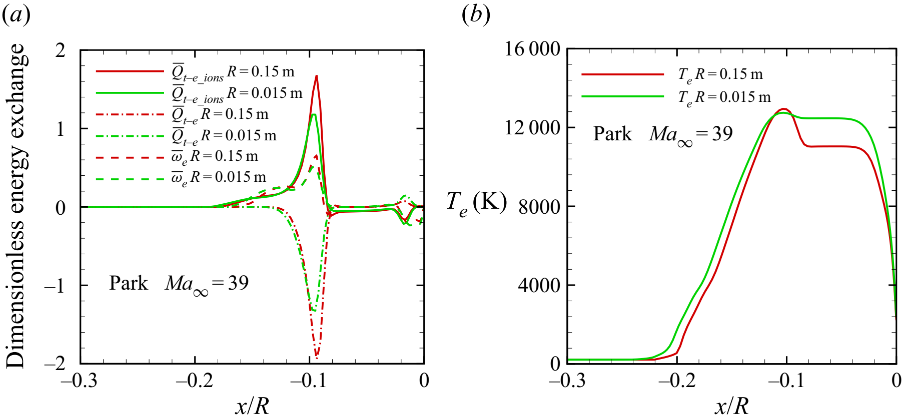

Figure 24. (a) Dimensionless energy exchange $\bar{Q}_{t-e\_ions}$, $\bar{Q}_{i-e}$ and $\bar{\omega}_e$ and (b) temperature T_e along the stagnation line at $Ma_\infty = 39$ with $\rho_\infty R = 1.3131 \times 10^{-5}$ kg m^{-2} using the Park model.

5. Conclusions

The applicability of the binary scaling law to electron distribution in thermochemical non-equilibrium flows at high altitude with high Mach number is investigated through theoretical analysis and numerical simulation in the present study. The main results show the following.

The binary scaling law is no longer applicable to electron distribution at extremely high Mach number even though the density of free stream is very low. In addition to the three-body reactions, the translation–electron energy exchange from collisions between electrons and ions Q_{t-e_ions} can theoretically lead to the invalidation of the binary scaling law. The vibrational energy change caused by Q_{t-v_m}, Q_{v-v_m} and Q_{e-v_m} cannot theoretically result in the failure of the binary scaling law.

As the Mach number increases, electron-impact ionization reactions can result in the failure of the binary scaling law. If the Gupta model is employed, $\mathrm{O} + \mathrm{e}^- \rightleftharpoons \mathrm{O}^+ + \mathrm{e}^- + \mathrm{e}^-$ is the main factor which causes the invalidation of the binary scaling law for electron distribution at $Ma_\infty = 27$. If the Park model is used, $\mathrm{N} + \mathrm{e}^- \rightleftharpoons \mathrm{N}^+ + \mathrm{e}^- + \mathrm{e}^-$ becomes the main factor for the failure of the binary scaling law at $Ma_\infty = 39$. The root cause is that the forward reaction rate coefficients of electron-impact ionization reactions increase rapidly due to an increase of electron–electronic excitation temperature, which further leads to an increase in concentration of electrons and ions. The increase in the concentration of electrons and ions causes the reverse reaction rates of electron-impact ionization reactions to increase to the same order of magnitude as those of the forward reaction, which leads to the invalidation of the binary scaling law for distribution of e^-. Based on previous researches, the parameters for electron-impact ionization reactions of the Park model might be more reliable than those of the Gupta model. The rates of electron-impact ionization reactions need further study because they can strongly affect the applicable range of the binary scaling law for modelling electron distribution.

The effect of dissimilarity caused by Q_{t-e_ions} can be negligible though free-stream velocity is at a high level ($Ma_\infty = 17,\ 27$). However, as the Mach number increases further ($Ma_\infty = 39$), Q_{t-e_ions} and Q_{i-e} are dominant in the electron–electronic energy source term, which means that the negative effect on the binary scaling law caused by Q_{t-e_ions} cannot be ignored. The trend of Q_{t-e_ions} is opposite to that of Q_{i-e} at $Ma_\infty = 39$ and the negative effects of the two on the similarity of source term can be offset in part to some extent. On the basis of understanding the mechanism for the failure of the binary scaling law in electron distribution, future work will focus on developing a method to quickly estimate the difference in peak electron number density between the scaled and original models. Future work will also involve quantifying the effects of Q_{t-e_ions} on the dissimilarity of electron distribution.

Acknowledgements. The authors would like to thank L. Leheng for his help with English writing and revision of this paper. We would also like to thank the referees for their helpful comments and suggestions.

Declaration of interests. The authors report no conflict of interest.

Author ORCIDs.
Xu Xu https://orcid.org/0000-0002-5465-0610.

Appendix A. Method of normalization

The non-dimensional variables are expressed as follows:

$$\bar{x}_j = \frac{x_j}{L}, \quad \bar{t} = \frac{t}{L/U_\infty}, \quad \bar{u}_i = \frac{u_i}{U_\infty}, \tag{A1a–c}$$

$$\bar{\rho} = \frac{\rho}{\rho_\infty}, \quad \bar{T}, \bar{T}_{v_m}, \bar{T}_e = \frac{T, T_{v_m}, T_e}{T_\infty}, \quad \bar{p} = \frac{p}{\rho_\infty U_\infty^2}, \tag{A2a–c}$$

$$\bar{E}, \bar{E}_{v_m}, \bar{E}_e = \frac{E, E_{v_m}, E_e}{U_\infty^2}, \quad \bar{H}, \bar{H}_s, \bar{H}_e = \frac{H, H_s, H_e}{U_\infty^2}, \tag{A3a,b}$$

$$\bar{\mu} = \frac{\mu}{\mu_\infty} = \frac{f_\mu(T, T_e, y_1, \ldots, y_{ns})}{\mu_\infty}, \tag{A4}$$

$$\bar{D}_s = \frac{D_s}{\mu_\infty/\rho_\infty} = \frac{{f'}_{D_s}(T, T_e, y_1, \ldots, y_{ns})/\rho}{\mu_\infty/\rho_\infty}, \tag{A5}$$

$$\left.\begin{aligned}
\bar{k}_{tr} &= \frac{k_{tr}}{\mu_\infty U_\infty^2/T_\infty} = \frac{f_{k_{tr}}(T, y_1, \ldots, y_{ns})}{\mu_\infty U_\infty^2/T_\infty} \\
\bar{k}_{v_m} &= \frac{k_{v_m}}{\mu_\infty U_\infty^2/T_\infty} = \frac{f_{k_{vm}}(T, T_{vm}, y_1, \ldots, y_{ns})}{\mu_\infty U_\infty^2/T_\infty} \\
\bar{k}_e &= \frac{k_e}{\mu_\infty U_\infty^2/T_\infty} = \frac{f_{k_e}(T, T_e, y_1, \ldots, y_{ns})}{\mu_\infty U_\infty^2/T_\infty}
\end{aligned}\right\}, \tag{A6}$$

where the functions $f_\mu, f'_{D_s}, f_{k_{tr}}, f_{k_{vm}}$ and f_{k_e} are described in § 2.5.

REFERENCES

Anderson, J.D.J.R. 2006 *Hypersonic and High-Temperature Gas Dynamics*, 2nd edn. American Institute of Aeronautics and Astronautics.

Appleton, J.P. & Bray, K.N.C. 1964 The conservation equations for a non-equilibrium plasma. *J. Fluid Mech.* **20** (4), 659–672.

Birkhoff, G. 1960 *Hydrodynamics: A Study in Logic, Fact and Similitude*, 2nd edn. Princeton University Press.

Birkhoff, G. & Eckerman, J. 1963 Binary collision modeling. *J. Math. Mech.* **12** (4), 543–556.

Blazek, J. 2015 *Computational Fluid Dynamics: Principles and Applications*. Butterworth-Heinemann.

Camm, J.C., Kivel, B., Taylor, R.L. & Teare, J.D. 1961 Absolute intensity of non-equilibrium radiation in air and stagnation heating at high altitudes. *J. Quant. Spectrosc. Radiat. Transfer* **1** (1), 53–75.

Candler, G.V. 1988 The computation of weakly ionized hypersonic flows in thermo-chemical nonequilibrium. PhD dissertation, Stanford University.

Candler, G.V. 2019 Rate effects in hypersonic flows. *Annu. Rev. Fluid Mech.* **51**, 379–402.

Candler, G.V. & MacCormack, R.W. 1991 Computation of weakly ionized hypersonic flows in thermochemical nonequilibrium. *J. Thermophys. Heat Transfer* **5** (3), 266–273.

Dunn, M.G. 1971 Measurement of $\mathrm{C}^+ + \mathrm{e}^- + \mathrm{e}^-$ and $\mathrm{CO}^+ + \mathrm{e}^-$ recombination in carbon monoxide flows. *AIAA J.* **9** (11), 2184–2191.

Dunn, M.G. & Kang, S.W. 1973 *Theoretical and Experimental Studies of Reentry Plasmas*, vol. 2232. National Aeronautics and Space Administration.

Ellington, D. 1967 Binary scaling limits for hypersonic flight. *AIAA J.* **5** (9), 1705–1706.

Farbar, E., Boyd, I.D. & Martin, A. 2013 Numerical prediction of hypersonic flowfields including effects of electron translational nonequilibrium. *J. Thermophys. Heat Transfer* **27** (4), 593–606.

Garicano-Mena, J., Lani, A. & Degrez, G. 2018 An entropy-variables-based formulation of residual distribution schemes for non-equilibrium flows. *J. Comput. Phys.* **362**, 163–189.

Ghezali, Y., Haoui, R. & Chpoun, A. 2019 Study of physico-chemical phenomena in a non-equilibrium hypersonic air flow behind a strong shock wave. *Thermophys. Aeromech.* **26** (5), 693–710.

Gibson, W.E. & Marrone, P.V. 1964 A similitude for non-equilibrium phenomena in hypersonic flight. In *AGARDograph*, vol. 68, pp. 105–131. Elsevier.

Gnoffo, P.A., Gupta, R.N. & Shinn, J.L. 1989 Conservation equations and physical models for hypersonic air flows in thermal and chemical nonequilibrium. *NASA Tech. Paper* 2867.

Gupta, R.N., Yos, J.M., Thompson, R.A. & Lee, K.P. 1990 A review of reaction and thermodynamic and transport properties for an 11-species air model for chemical and thermal nonequilibrium calculations to 30000K. *NASA Tech. Rep.* 1232.

Hall, J.G., Eschenroeder, A.Q. & Marrone, P.V. 1962 Blunt-nose inviscid airflows with coupled nonequilibrium processes. *J. Aerosp. Sci.* **29** (9), 1038–1051.

Hao, J., Wang, J. & Lee, C. 2016 Numerical study of hypersonic flows over reentry configurations with different chemical nonequilibrium models. *Acta Astronaut.* **126**, 1–10.

Hornung, H.G. 1972 Non-equilibrium dissociating nitrogen flow over spheres and circular cylinders. *J. Fluid Mech.* **53** (1), 149–176.

Hornung, H.G. 1988 28th Lanchester memorial lecture—experimental real-gas hypersonics. *Aeronaut. J.* **92** (920), 379–389.

Houwing, A.F.P., Nonaka, S., Mizuno, H. & Takayama, K. 2000 Effects of vibrational relaxation on bow shock standoff distance for nonequilibrium flows. *AIAA J.* **38** (9), 1760–1763.

JONES, W.L. & CROSS, A.E. 1972 Electrostatic-probe measurements of plasma parameters for two reentry flight experiments at 25000 feet per second. *Rep. no.* 6617. National Aeronautics and Space Administration.

KIM, S.D., LEE, B.J., LEE, H.J. & JEUNG, I.S. 2009 Robust HLLC Riemann solver with weighted average flux scheme for strong shock. *J. Comput. Phys.* **228** (20), 7634–7642.

LANDAU, L. & TELLER, E. 1936 Theory of sound dispersion. *Phys. Z. Sowjetunion* **10**, 34–43.

LEE, J.H. 1984 Basic governing equations for the flight regimes of aeroassisted orbital transfer vehicles. In *19th Thermophysics Conference, Snowmass, Colorado, AIAA Paper* 84-1729.

LEE, J.H. 1993 Electron-impact vibrational relaxation in high-temperature nitrogen. *J. Thermophys. Heat Transfer* **7** (3), 399–405.

LEE, R.H. & BAKER, R.L. 1969 Binary scaling of air ionization on slender cones at small yaw. *AIAA J.* **7** (2), 355–358.

MARSCHALL, J. & MACLEAN, M. 2011 Finite-rate surface chemistry model, I: formulation and reaction system examples. In *42nd AIAA Thermophysics Conference, Honolulu, Hawaii, San Diego, CA, AIAA Paper* 2011-3783.

MATSUZAKI, R. 1988 Quasi-one-dimensional aerodynamics with chemical, vibrational and thermal nonequilibrium. *Trans. Japan Soc. Aeronaut. Space Sci.* **30**, 243–258.

MEN'SHOV, I.S. & NAKAMURA, Y. 2000 Numerical simulations and experimental comparisons for high-speed nonequilibrium air flows. *Fluid Dyn. Res.* **27** (5), 305–334.

MILLER, J., TANNEHILL, J., LAWRENCE, S. & EDWARDS, T. 1995 Development of an upwind pns code for thermo-chemical nonequilibrium flows. In *30th AIAA Thermophysics Conference, AIAA Paper* 95-2009.

MILLIKAN, R.C. & WHITE, D.R. 1963 Systematics of vibrational relaxation. *J. Chem. Phys.* **39** (12), 3209–3213.

MUYLAERT, J., WALPOT, L., HÄUSER, J., SAGNIER, P., DEVEZEAUX, D., PAPIRNYK, O. & LOURME, D. 1992 Standard model testing in the European high enthalpy facility F4 and extrapolation to flight. In *17th Aerospace Ground Testing Conference, Nashville, TN, AIAA Paper* 92-3905.

NIU, Q., YUAN, Z., DONG, S. & TAN, H. 2018 Assessment of nonequilibrium air-chemistry models on species formation in hypersonic shock layer. *Intl J. Heat Mass Transfer* **127**, 703–716.

OZAWA, T., ZHONG, J. & LEVIN, D.A. 2008 Development of kinetic-based energy exchange models for noncontinuum, ionized hypersonic flows. *Phys. Fluids* **20** (4), 442–165.

PARK, C. 1968 Measurement of ionic recombination rate of nitrogen. *AIAA J.* **6** (11), 2090–2094.

PARK, C. 1973 Comparison of electron and electronic temperatures in recombining nozzle flow of ionized nitrogen—hydrogen mixture. Part 1. Theory. *J. Plasma Phys.* **9** (2), 187–215.

PARK, C. 1985 Convergence of computations of chemical reacting flows. *Prog. Astronaut. Aeronaut.* **103**, 478–513.

PARK, C. 1990 *Nonequilibrium Hypersonic Aerothermodynamics*. Wiley.

PARK, C. 1993 Review of chemical-kinetic problems of future NASA missions. I-earth entries. *J. Thermophys. Heat transfer* **7** (3), 385–398.

PARK, C. & LEE, S.H. 1995 Validation of multitemperature nozzle flow code. *J. Thermophys. Heat Transfer* **9** (1), 9–16.

PARK, J.S., YOON, S.H. & KIM, C. 2010 Multi-dimensional limiting process for hyperbolic conservation laws on unstructured grids. *J. Comput. Phys.* **229** (3), 788–812.

PETSCHEK, H. & BYRON, S. 1957 Approach to equilibrium ionization behind strong shock waves in argon. *Ann. Phys.* **1**, 270–315.

RAMJATAN, S., LANI, A., BOCCELLI, S., HOVE, B.V., KARATEKIN, Ö, MAGIN, T. & THOEMEL, J. 2020 Blackout analysis of Mars entry missions. *J. Fluid Mech.* **904**, A26.

ROBERTS, T. 1994 The development of a multi-vibrational model and incorporation into a chemical reacting Navier-Stokes solver. In *6th AIAA/ASME Joint Thermophysics and Heat Transfer Conference, Colorado Springs, CO AIAA Paper* 94-1988.

ROBERTS, T. 1996 Implementation into TINA modelling for electron/electronic energy equation. In *31st AIAA Thermophysics Conference, New Orleans, LA, AIAA Paper* 96-1851.

SCALABRIN, L.C. 2007 Numerical simulation of weakly ionized hypersonic flow over reentry capsules. PhD dissertation, University of Michigan.

SHEN, C. 2005 *Rarefied Gas Dynamics: Fundamentals, Simulations and Micro Flows*. Springer Science & Business Media.

SIVOLELLA, D. 2014 *To Orbit and Back Again: How the Space Shuttle Flew in Space*. Springer.

TEARE, J.D., GEORGIEV, S. & ALLEN, R.A. 1962 Radiation from the non-equilibrium shock front. In *Hypersonic Flow Research*, pp. 281–317. Elsevier.

THOENES, J. 1969 Inviscid hypersonic flow of chemically relaxing air about pointed circular cones. *UARI Res. Rep.* 66, Alabama Univ, Huntsville, AL.

WILKE, C.R. 1950 A viscosity equation for gas mixtures. *J. Chem. Phys.* **18** (4), 517–519.

ZENG, M. 2007 Numerical rebuilding of free-stream measurement and analysis of nonequilibrium effects in high-enthalpy tunnel. PhD dissertation, Institute of Mechanics, CAS (in Chinese).

ZENG, M., LIN, Z., LIU, J. & QU, Z. 2009 Numerical analysis of the validity of binary scaling parameter $\rho_\infty L$ in nonequilibrium flow. *Chin. J. Theor. Appl. Mech.* **41** (2), 177–184 (in Chinese).

ZHANG, H.X. 1990 The similarity law for real gas flow. *Acta Aerodyn. Sin.* **8** (1), 1–8 (in Chinese).

ZHANG, F., LIU, J. & CHEN, B. 2018 Modified multi-dimensional limiting process with enhanced shock stability on unstructured grids. *Comput. Fluids* **161**, 171–188.

ZHU, Y., LEE, C., CHEN, X., WU, J., CHEN, S. & GAD-EL-HAK, M. 2018 Newly identified principle for aerodynamic heating in hypersonic flows. *J. Fluid Mech.* **855**, 152–180.